Long-term sediment yields from glacierized basins on Mount Baker, 1947-2015

Eli Schwat

A thesis

submitted in partial fulfillment of the

requirements for the degree of

Master of Science in Civil Engineering

University of Washington

2022

Committee:

Erkan Istanbulluoglu

Alexander Horner-Devine

Program Authorized to Offer Degree:

Civil and Environmental Engineering

University of Washington

Abstract

Long-term sediment yields from glacierized basins on Mount Baker, 1947-2015

Eli Schwat

Chair of the Supervisory Committee

Erkan Istanbulluoglu

Civil and Environmental Engineering

Where glacierized watersheds are adjacent to population centers, sediment-laden rivers may catastrophically flood and the frequency of such flooding has been predicted to increase along with increased sediment supply. Despite these concerns, upland sources of sediment and sediment connectivity between proglacial uplands and downstream river plains are poorly understood. We utilize automated Structure from Motion software to process historical aerial imagery and, in tandem with publicly available LIDAR data, produce a DEM time series with coverage that spans from 1947 to 2015 in glacierized watersheds on Mount Baker, a stratovolcano in Washington State. We measure basin-wide sediment yields in 10 distinct basins and quantify the relative sediment contributions of different upland erosion processes. Sediment yields are correlated with lithology, Little Ice Age moraine slope, upslope contributing area, and glacier retreat. We found that upslope contributing area and moraine slope are the strongest predictors of basin-wide sediment yield, and stream channel slope is a poor predictor of sediment yield, indicating that debris flows originating from glacier moraines are a primary erosion

mechanism in proglacial basins. Our estimates of proglacial sediment yields account for 10 to 56% of estimated total sediment load in the Nooksack river, which drains multiple basins on Mount Baker, and sediment input from proglacial basins exceed contributions from erosion of glacial and volcanic terraces. On intra-decadal timescales, the irregularity of hillslope erosion events disconnect proglacial sediments from the downstream system. On decadal timescales, infrequent debris flows bypass proglacial stream channels and carry sediment downstream of proglacial limits. Our findings indicate that pro-glacial sediments may contribute a significant portion of riverine sediments where upland topography and lithology are favorable and when the climate is relatively wet.

1. Introduction

Understanding the transport of sediment on steep slopes is critical to the assessment of geohazard risks on engineering timescales and the characterization of landscape evolution over geomorphic timescales. Characterizing erosion processes in glacierized mountain ranges is especially challenging. Field study is limited by difficult access and climate change and glacier fluctuations may modify erosion rates and geohazard risk (Carrivick and Heckmann, 2017; Legg et al., 2014). As glaciers retreat, oversteepened hillslopes are debutressed, moraines become unstable, and drainage networks expand upslope, increasing catchment-scale sediment connectivity (Lane et al, 2017). Both climate and historical glacial extents have been shown to control erosion rates. Relict glacial landforms, which have been undergoing relaxation since the end of the Little Ice Age (LIA), are eroded when intense rainstorms and prolonged wet periods initiate landslides and debris flows (Lancaster et al., 2012; Legg et al.; Carrivick and Heckmann).

Upland erosion rates and catastrophic debris-flow and landslide events remain difficult to predict. Recently, models have been used to estimate landsliding probabilities over large spatial extents (Strauch et al, 2019) and experiments have been performed to understand the dominant physical drivers of steep-slope sediment motion on the grain scale (Prancevic et al, 2014). Steep-slope erosion study sites vary from forested basins (Istanbulluoglu et al., 2013) to proglacial basins (Lancaster et al., 2012; Legg et al., 2014). Increasingly widespread access to high-resolution topographic datasets (e.g. airborne LIDAR and Structure from Motion (SfM) photogrammetry) is allowing measurement in settings where field measurements were previously impossible. Cody et al. (2020) use LIDAR and SfM to examine how sliding and debris flows follow glacial debuttressing in New Zealand and find that displaced sediment volumes from paraglacial systems have likely been underestimated. A comparison of four deglaciating basins on Mount Rainier, a large stratovolcano in the Pacific Northwest (PNW) of the continental United States, demonstrates that coarse sediment yield varies from basin to basin as a function of valley geometry and that deglaciating basins are mostly disconnected from downstream river systems over decadal time scales (Anderson and Shean, 2022). Lancaster et al. (2012) found that a suite of debris flow initiation sites on Mount Rainier are all located in areas exposed by glacial retreat since the LIA and were differentiated from non-debris flow sites by large upslope contributing areas. Legg et al. (2014) examined the same initiation sites and found that gully heads all had slopes greater than 19˚ and that debris-flow frequency may increase with continued glacial retreat due to the positive slope-elevation relationship on Mount Rainier. The influence of long-term glacial retreat on erosion rates may also be complicated by the fact that many glaciers in the PNW experienced periods of advance during the 20th century (Dick, 2013; Harper, 2013).

Understanding erosion rates in glacierized mountain landscapes is also important for understanding natural systems downstream. In glacierized river systems near population centers (e.g. the PNW, European alps), sediment-laden rivers may catastrophically flood, and the frequency of such floods has been predicted to increase along with increased sediment supply (Beason et al., 2011, Lee and Hamlet, 2011). Despite the possibility that proglacial sediments instigate stream channel aggradation and flooding (Anderson and Konrad, 2019; Ahrendt et al., 2022), the relative contribution of proglacial sediments at the river basin scale remains unclear. Anderson and Konrad (2019) hypothesize that a downstream-propagating sediment wave initiated in glacierized basins on Mount Baker in response to cooler-wetter weather in the 1940s

and 1950s. Ahrendt et al. (2022) found that aggradation and changes to streambed elevation are likely contributors to flood risk in Western Washington.

In flood-prone river basins sourced from glacierized mountains, the following research questions are critical for improving our understanding of proglacial erosion processes, geohazard risk, sediment yields and their impact on local flooding:

1. What are the dominant erosion processes in proglacial landscapes and what are their relative contributions to proglacial basin sediment yields?
2. What factors control the magnitude and temporal and spatial variability of erosion rates and sediment yields in proglacial basins?
3. What is the relative contribution of proglacial sediments at the river basin scale?

We study these questions in a number of proglacial basins on Mount Baker, a glacierized stratovolcano in Washington State that feeds the unregulated North and Middle forks of the Nooksack River. We use recently developed Historical Structure from Motion (HSfM) processing software (Knuth et al., in review) and produce a time series of Digital Elevation Models (DEMs) that allow precise measurement of land surface change between 1947 and 2015. In each glacierized valley we measure decadal erosion rates and sediment yields and identify the location of landslides, gully erosion, and stream channel erosion.

2. Study Area

Mount Baker is an active, andesitic stratovolcano in the Cascade Volcanic Arc with a summit elevation of 3,286 meters (Wood and Kienle, 1990; Scott et al, 2005). Mount Baker is the second most glacierized volcano in Washington state, after Mount Rainier. The Deming, Thunder, Coleman, Roosevelt, and Mazama glacier valleys feed into the north and middle forks of the Nooksack river, which flows west and empties into Bellingham Bay (Figure 1). The remaining watersheds feed into the man-made Baker Lake and Lake Shannon reservoirs, both part of the Skagit River watershed. The Nooksack river has recently experienced significant flooding with associated costs approaching $50 million in Whatcom County of Washington state alone (Associated press, 2021). Concurrent flooding in British Columbia had estimated economic costs of $2 billion (Dalton, 2021).

Mount Baker's glaciers have generally been retreating since the LIA glacial maxima in the eighteenth and nineteenth centuries. The glaciers rapidly retreated between 1930 and 1945, advanced between 1945 and 1980, and most have been retreating since 1980 (Dick, 2013; Harper, 2013). Figure 1 shows the fluctuation of observed glacier extent since 1947. In 2015, most glaciers had footprints similar to those in 1947, with additional retreat observed for the Mazama and Deming glaciers. The LIA lateral moraines approximately represent the margins of glaciers during their LIA maxima (Figure 1).

Sediments sourced from Mount Baker have been identified as the potential cause of downstream aggradation in the Nooksack River (Anderson and Konrad, 2019) and modern observations have identified debris flows as a primary mechanism transporting upland sediments downstream (Fuller, 1980; Tucker et al., 2014; Legg et al., 2014). A large "ice and boulder avalanche" flowed

from Deming glacier in June 1927, transporting approximately 10 million m^3 of material and traveling 9.5 - 12 km downstream (Fuller, 1980; Tucker et al., 2014). This event deposited some debris 1.5 km downstream of the 2015 glacier terminus; the Upper Middle Fork Nooksack river has since incised into this deposit, forming 15 to 20 meter tall terraces. Tucker et al. report the occurence of two other modern debris flows originating near Deming glacier. One debris flow on May 31, 2013 originated as a landslide on the LIA moraine north of the 2013 glacier terminus, moved approximately 100,000 m^3 of material and ran out 5.6 to 8.8 km. A second debris flow occurred on June 6, 2013 and originated as a landslide on the north side of the 1927 debris flow deposit (Tucker et al., 2014). Tucker et al. note that deposits from the 2013 debris flows had eroded significantly within three weeks of the events, indicating that evidence of similarly sized debris flows may erode beyond recognition within a few years. Tucker et al. also hypothesize two debris flow events occurred in October 2003 and sometime in 2008. Fuller (1980) reports two historical debris avalanches originating near Rainbow glacier; one event occurred in the early 1860s and one in 1888. These events deposited material downstream of Rainbow glacier's LIA terminus and the deposits are clearly identifiable in the LIDAR data.

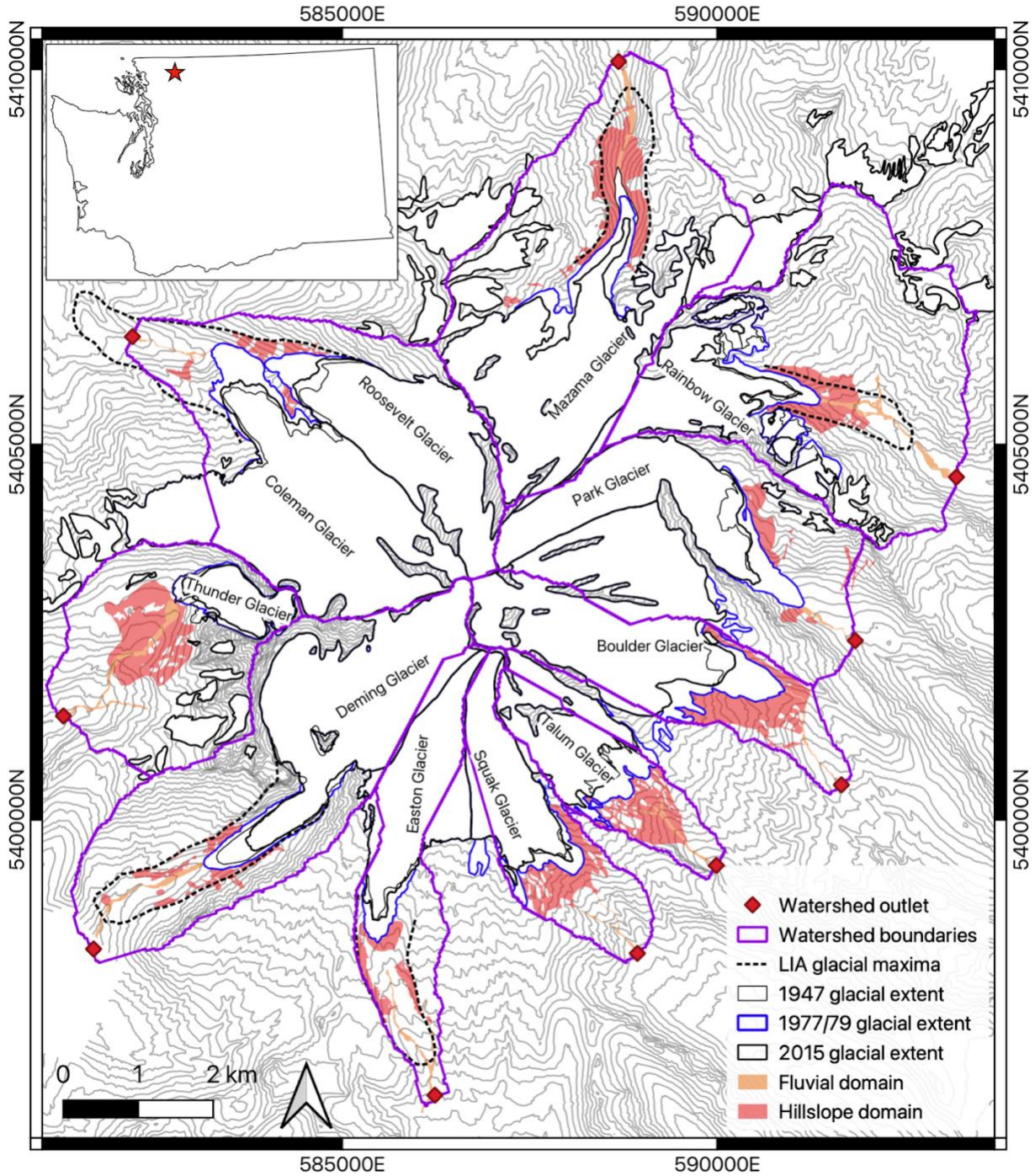

Figure 1. Context map for Mount Baker with glacier outlines, manually delineated fluvial and hillslope erosion domains, overlaid on 50 meter contours derived from 2015 LIDAR DEM. The LIA glacial maximum for Mazama glacier is inferred from topography; all other LIA maxima are from Roe and O'Neal (2009). For all named glaciers, boundaries are shown for 1947, 1979, and 2015; for Rainbow glacier the 1977 glacier boundary is shown instead of 1979. Glacier extents are modified from the Randolph Glacier Inventory (RGI Consortium, 2017) boundaries. For unnamed glaciers, the original boundaries from the RGI dataset are shown, represented with the 2015 glacial extent symbol. The inset figure shows the location of Mount Baker within Washington State.

3. Methods

To address our research questions, we must determine the spatial and temporal patterns of erosion, measure volumetric change attributable to different erosion processes, and characterize glacier behavior. These measurements can be extracted from precise surface elevation change measurements using high-resolution DEM time series for Mount Baker. We then identify distinct watersheds on Mount Baker, identify exposed areas within those watersheds where elevation change due to erosion can be measured, and identify changing glacier boundaries. We then measure volumetric erosion rates by differencing DEMs for available time periods and we estimate associated uncertainty. Finally, we characterize the topography of each glacierized watershed and correlate these characteristics with erosion rates using geomorphic transport laws drawn from and inspired by the literature. The following sections provide additional details for each of the above steps.

3.1 Preparing a DEM time series

3.1.1 Historical Structure from Motion (HSfM)

We used structure from motion to derive DEMs from historical aerial imagery. We downloaded scanned historical aerial photographs taken in 1947 from the USGS EarthExplorer data portal (EE). These images were collected in an overlapping grid pattern from an altitude of 6000 meters, provide complete coverage of Mount Baker, and have an average ground sample distance of 1 meter. We also downloaded all available scanned historical aerial photographs acquired between 1970 and 1992 as part of the USGS North American Glacier Aerial Photography (NAGAP) program from the NSF Arctic Data Center (Nolan et al., 2017). These images were captured from variable altitudes and have an average ground sample distance of 30 cm. The NAGAP imagery was generally collected for single flight lines oriented along the glacier centerlines, with coverage over the lower glacier and forefield. When combined, NAGAP photographs taken in 1977 and 1979 provide nearly complete coverage of Mount Baker.

We generated Digital Elevation Models (DEMs) from scanned historical aerial single frame photographs using the Historical Structure from Motion (HSfM) software package (Knuth et al., 2021b) and methodology described in Knuth et al. (in review). Generated DEMs are posted at 2 meters. Scanned images were downloaded and standardized using the Historical Image Preprocessing (HIPP) software package (Knuth et al., 2021a). Image acquisition dates span from 1947 to 1992 and all images were captured during August, September, or October, when seasonal snowpack was minimal or nonexistent. We used a 2015, LIDAR-based Digital Surface Model (DSM) available from the Washington DNR LIDAR portal (Ramsey, 2016) as the reference DEM required by HSfM. This dataset was obtained from flights between August and September of 2015 and has a posting of 1 meter. We approximate the LIDAR collection date as September 1, 2015 throughout this study.

3.1.2 Associated Imagery

In addition to a DEM, the HSfM software produces an orthomosaic from each single-date collection of aerial photographs between 1947 and 1992. We downloaded imagery collected on

9/28/2015 as part of the National Agriculture Imagery Program (NAIP, retrieved from EE) to aid analysis of 2015 LIDAR data. These imagery are used to aid in the delineation of glacier boundaries (Section 3.2.3), geomorphic process domains (Section 3.2.2) and to identify areas of stable ground (Section 3.4).

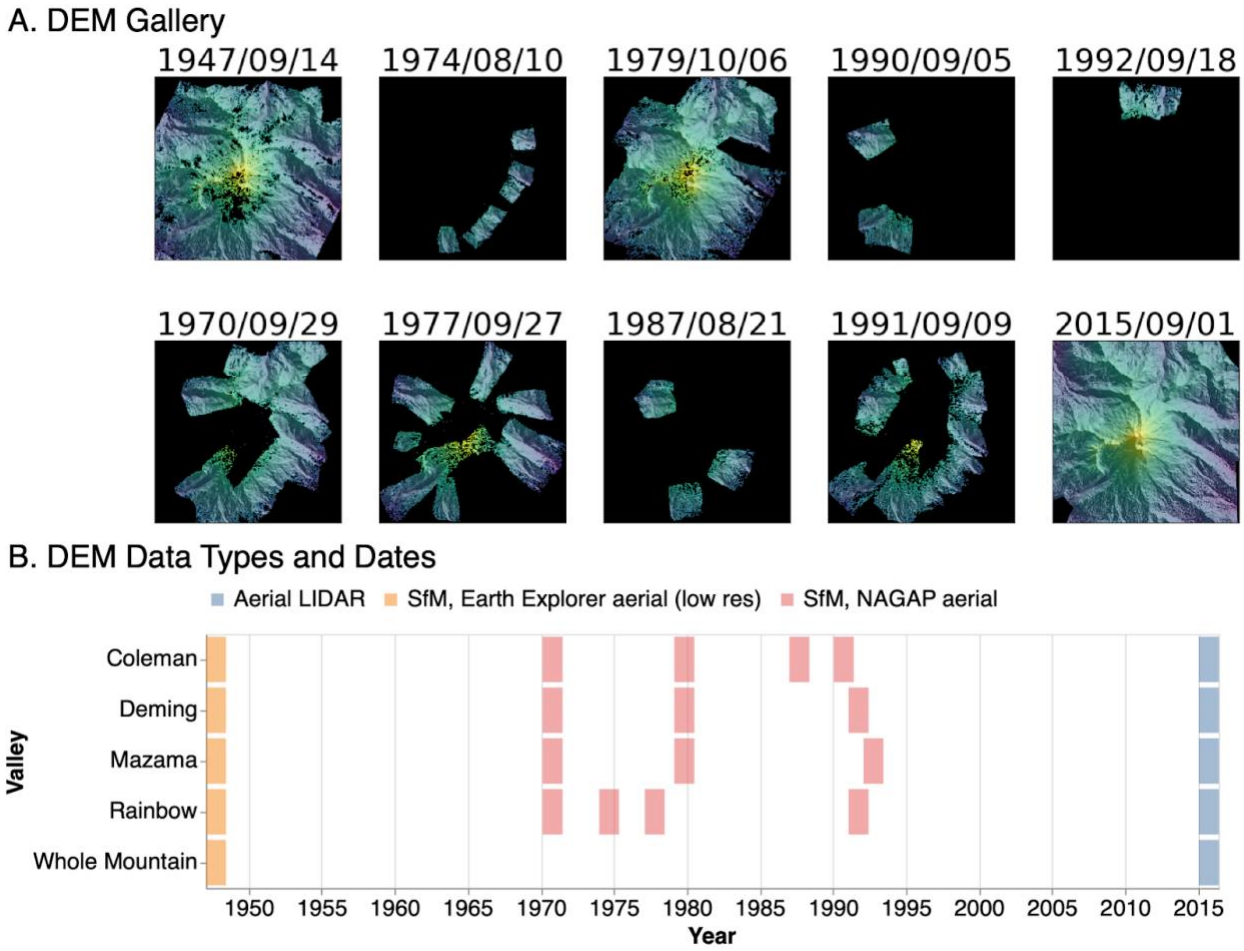

Figure 2. (A) Illustration of the DEM datasets used for analysis in individual valleys and for analysis over all of Mount Baker. Types/source of imagery shown in color. Black outlines indicate DEMs with coverage over a larger area. (B) All DEMs used in this analysis, showing how spatial coverage varies from year to year.

3.2 Basin and measurement area definition

3.2.1 Watershed boundaries

For 10 glacierized basins on Mount Baker (referred to by the name of their glaciers, Figure 1), we manually identified watershed outlet points within the stream channel at the downstream extent of the 1947 DEM coverage (Figures 1 and 2). We use these watershed outlet points to automatically delineate watershed boundaries using the StreamStats web tool (U.S. Geological Survey, 2016) (Figure 1).

3.2.2 Delineation of landscape process domains for change detection

Within each watershed we manually delineated different landscape process domains using DEMs, orthomosaics, and NAIP imagery (Section 3.1). These include a fluvial domain, a hillslope domain, and process-specific areas including erosion due to mass wasting, gully erosion, and glacial change.

The fluvial domain polygons include the primary stream channel, extending from the modern glacier terminus to the watershed outlet point. The stream channel was mapped from bank to bank, with banks identified by sharp convex topography and, in some cases, a vegetation boundary.

We create hillslope domain boundaries by manually outlining as much exposed (unvegetated) area as possible, outside of the fluvial domain, where our DEM dataset has repeat coverage and where bareground is defined as having been unvegetated at any point during our study period. Hillslope domains generally include all unvegetated land areas within LIA glacial maxima moraines, where such moraines are visible. In watersheds with sparse tree growth (Easton, Squak, Talum, Boulder, and Park watersheds), sparsely vegetated areas are included because positive elevation change signals attributable to sparse tree growth are expected to be insignificant. Note that we do not expect to observe geomorphic change due to hillslope diffusive processes, such as soil creep and bioturbation, which cause elevation change of a magnitude that is not detectable within the accuracy of our DEMs and over our measurement time period.

To quantify the relative dominance of different erosion types, we delineate "process polygons", areas within the hillslope and fluvial domains where we assign an erosion category, such as mass wasting, gully, and glacial erosion, based on landscape context. To do so, we first visually inspect orthomosaics and DEMs of Difference (DoDs, see Section 3.3.1) and identify eroded areas with significant negative elevation change, and manually outline them. Mass-wasting polygons include landslide and rockfall erosion processes; landsliding polygons are characterized by hollow and concave-converging topography and rockfall areas are characterized by convex hillslope/moraine tops. Gully process polygons include areas of channelized erosion, outside the fluvial domain, characterized by concave, V-shaped cross-sectional geometry, often with evidence of an ephemeral stream. Glacial process polygons include any erosion signals that appear to be directly caused by glacier movement observed during our study time period. These erosion signals may be due to glacial debutressing, whereby material adjacent to a glacier boundary fails after the glacier retreats, or quarrying and plucking, whereby a glacier advances and retreats over a land surface, redistributing or incorporating material as it moves.

Manual delineation of the hillslope and fluvial domains and mass wasting and gully polygons is validated by examination of topographic characteristics within the delineated areas (Figure 3, Section 3.5). Fluvial domains have lower slopes than hillslope domains (Figure 3A). Within the fluvial domains, slope generally decreases with increasing drainage area, but there is a second peak in slope at high drainage areas (approximately 2 million m^2). This second peak represents a change from low stream channel gradient within the LIA glacial limits to a relatively high gradient downstream of LIA glacial limits in Deming, Rainbow, Mazama, Coleman/Roosevelt, and Park glacier valleys. Gully and mass-wasting process areas have similar slopes. Nearly all of the gully and mass-wasting sites have slopes within the debris-flow slope range (> 34˚) identified

experimentally by Prancevic et al. (2014). Gullies have higher upslope drainage areas and more concave-convergent geometries, as a result of flow-driven incision (Figure 3B).

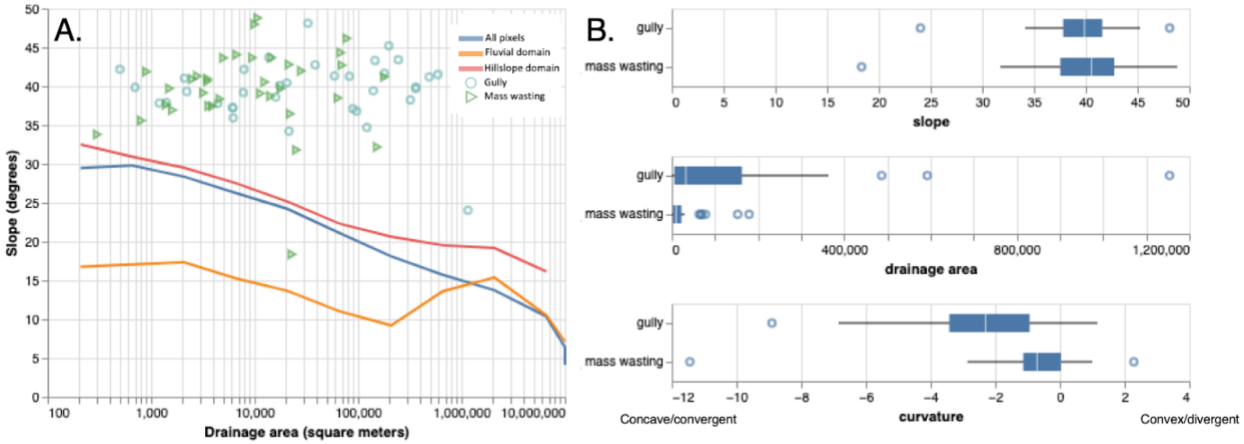

Figure 3. (A) Distribution of slope and drainage area values extracted from the 2015 DTM. Lines show the median slope values for bins of drainage area for all pixels in the 2015 DTM (blue line), all pixels in the fluvial process domains (orange line), and all pixels in the hillslope process domain (red line). Points show the maximum drainage area value and mean slope value of all pixels within each separate gully erosion polygon (blue circles, n = 35) and mass wasting polygon (green triangles, n = 35). (B) Distributions of slope, drainage area, and curvature values extracted from the 2015 DTM for gully and mass-wasting polygons. The slope raster is generated using the Horn (1981) algorithm and the curvature raster using the Zevenbergen and Thorne (1987) algorithm, both implemented in the xDEM software package (xDEM Contributors, 2021). The drainage area raster is generated using the Pysheds software package (Bartos et al., 2022).

3.2.3 Glacier polygons

We delineate glacier outlines to characterize glacier behavior over our study time period and to identify change signals that should not be included in any mass wasting measurements. We created glacier outlines for Mt. Baker by modifying polygons from the Randolph Glacier Inventory (RGI), a global database of glacier outlines (RGI Consortium, 2017). For each of the 11 named glaciers (Figure 1), we manually modified the base RGI outline polygon to record the evolving glacier extent in each of the available historical orthoimage mosaics. In some years and watersheds, large patches of snow remain near glaciers. These are included in the glacier outline to exclude accumulation and melting snow signals in our measurements. Most glaciers on Mount Baker were at their maximum extents in the late 1970s. When we calculate glacial retreat (Section 3.5) we use 1979 glacier boundaries for all glaciers except Rainbow and Park, for which 1979 coverage is limited and 1977 glacier boundaries are substituted.

3.3 Measuring landscape change

To analyze geomorphic change across multiple time intervals, we calculate elevation change for pairs of DEMs to create DEM of Difference (DoD) products. We then calculate net volumetric change and, for comparison, gross positive and negative volumetric changes within the fluvial and hillslope domains and within the process polygons.

3.3.1 Creating time series of DEMs of Difference (DoD)

To prepare DEMs for differencing, we coregistered historical DEMs to the reference 2015 DEM using an iterative process handled by HSfM involving point cloud alignment (implemented in the NASA Ames Stereo Pipeline; Beyer et al., 2019, 2018; Shean et al., 2016) and Nuth and Kääb (2011) coregistration (Shean et al., 2021). We reprojected the 2015 LIDAR dataset to 2 meter resolution, reprojected all other DEMs to match the grid and resolution of the 2 meter LIDAR dataset, and computed DoD products.We perform two post-processing steps to improve DoD data quality. First, we remove outliers with elevation change values outside the range -50 to 50 meters, which is the magnitude of the largest negative observed geomorphic change between 1947 and 2015. Second, we interpolate across data gaps in the DoDs by applying a linear interpolation algorithm with a maximum lateral search distance of 50 meters (Xdem Contributors, 2021), which is sufficient to fill all data gaps in the measurement areas. All DoDs used in this study and their errors are listed in Table 1.

We map long-term geomorphic change (68 years) across the whole mountain by differencing the 1947 and 2015 DEMs. The difference map revealed that most geomorphic activity occurred within the Mazama, Rainbow, Deming, and Coleman/Roosevelt proglacial zones during this period. We performed additional analysis on these four "high erosion sites" to investigate the drivers of greater geomorphic activity using additional DEMs between 1947 and 2015 (Figure 2A, B).

3.3.2 Calculating net and gross volumetric change

For the 10 watersheds, we measure net volumetric change within the combined hillslope and fluvial domains using the 1947-2015 DoD (Figure 2A, "Whole Mountain"). For the 4 high erosion sites, we measure net and gross volumetric change within the hillslope domain, the fluvial domain, and the process polygons using the DoD time series (Figure 2A). When measuring volumetric change with a DoD, we exclude ice and snow signals using glacier outlines from the DoD start and end dates. Net volumetric change is calculated as the mean elevation change value multiplied by measurement area. Gross positive (negative) volumetric change is calculated as the sum of all positive (negative) DoD pixels in a given area multiplied by pixel area. For gross change measurements, DoD values are thresholded at the 90% confidence level (Anderson, 2019; Anderson and Shean, 2022). We also present measurements of sediment yield in units of tonnes. To calculate sediment yields, we convert our measurements of volume, *V*, to mass, *M*, by approximating the porosity, *n*, of the source material as 0.35 (i.e., moraine material, Burki et al., 2010; Humlum, 2000) and the rock density, ρ_{rock}, as 2600 kg/m^3,

$$M = V(1-n)\rho_{rock} \qquad (1)$$

Reported net volumetric change and sediment yield measurements represent storage changes within the exposed areas of the watershed. We cannot quantify storage changes within the entire basin due to glacier and vegetation cover and limited DEM time series coverage. We also cannot confidently quantify supra- or subglacial sediment change. Considering these limitations, our net volumetric change and sediment yield measurements represent conservative, minimum estimates of the total sediment flux passing the watershed outlets.

3.4 Uncertainty Estimation

To estimate the uncertainty associated with measurements of volumetric change, we first identified areas of stable ground within the DoDs where true elevation change is negligible. To identify such areas we use orthomosaics and NAIP imagery between 1947 and 2015 (Figure S1). We then estimated the errors of each DoD and calculated errors associated with each volumetric change measurement. No effort was made to exclude areas of measurement from the stable ground areas (Anderson and Shean, 2022).

For each DoD, we calculated the root mean square (RMS), σ_{rms}, and the mean, σ_{sys}, of elevation change values over stable ground. We then generated an empirical spatio-variogram from elevation change values over stable ground and fitted a spherical variogram model with no nugget (Rolstad et al, 2009) and calculated the range, a_i, and sill, σ_{sc}. Results from the uncertainty analyses are presented in Table 1.

For a given volume change measurement made with a given DoD, we estimated the volumetric uncertainty, σ_v, using an error model that includes random error, systematic error, and spatially correlated error:

$$\sigma_v = nL^2 \sqrt{\frac{{\sigma_{rms}}^2}{n} + \frac{{\sigma_{sc}}^2}{n}\frac{\pi {a_i}^2}{5L^2} + \sigma_{sys}^2} \qquad (2)$$

where n is the number of pixels in a measurement and L is the DoD resolution (2 meters) (Anderson, 2019).

3.5 Explanatory terrain characteristics

To explore connections between observed erosion and terrain characteristics at the watershed scale, we calculate several terrain parameters, including the drainage area (upslope contributing area of each extracted watershed), A, channel slope, S_c, mean hillslope domain slope, S_h, glacial retreat area, ΔA_g, and nonigneous fraction, F_{ni} for each watershed. Channel slope is the difference between the elevation at the watershed outlet point and the elevation where the channel meets the maximum glacier terminus, divided by the length of the channel between the two points. Hillslope domain slope is the mean surface slope in the hillslope domain derived from a 2015 LIDAR Digital Topography Model (DTM) downsampled to 10 meter resolution (Ramsey, 2016). Glacial retreat area is the difference in glacial area between 1977/1979 and 2015, a period during which all glaciers retreated. Nonigneous fraction is the proportion of area within the hillslope and fluvial domain polygons not underlain by igneous bedrock lithology. Lithologies are extracted from a bedrock geologic map (Tabor et al., 2003).

3.6 Watershed sediment yield equations

We test a number of geomorphic transport power laws by modeling sediment yield (Q_s) as a function of terrain characteristics. Empirical relationships between erosion rate and topography have long been studied by geomorphologists at watershed, channel reach, and local hillslope scales. Relationships developed for channel reach or local scales are often referred to as geomorphic transport laws (GTLs) and are commonly used in landscape evolution models (e.g., Istanbulluoglu, 2009). GTLs can relate both local supply-limited erosion or global transport-

limited sediment flux to local variables, such as drainage area, slope, topographic curvature, erodibility, and substrate size (Dietrich et al., 2003). Popular forms of GTLs include the slope dependent (linear and non-linear) hillslope diffusion models used for soil creep and small-scale landslides, and area and slope dependent non-linear power-law river incision models (e.g., Stock and Montgomery, 1999). At the watershed scale, empirical relationships relate average erosion rate to channel slope, relief, and precipitation (Ahnert, 1970; Henck et al., 2011; Portenga and Bierman, 2011). In tectonically active settings with steep, near-threshold slopes, slope dependent GTLs have also been successfully applied to calculate watershed-scale erosion (Montgomery and Brandon, 2002).

In this study, we develop linear and non linear empirical equations for watershed-scale sediment yield inspired by GTLs, but implemented using spatially averaged topographic and environmental variables (Section 3.5). As the first step in developing such models, we correlate terrain characteristics A, S_c, S_h, A_g, and F_{ni} to measured sediment yield, and report the Nash-Sutcliffe model efficiency (NSE) of a simple linear model and a power law model of the form

$$Q_s = kA^m \qquad (3)$$

where Q_s is mean annual sediment yield (ton/y) calculated from the net volumetric change measured in the combined hillslope and fluvial domains and where A may be replaced by S_c, S_h, A_g, or F_{ni}. In the case of the linear model fits, NSE represents the proportion of variance explained by each variable (i.e. r^2). We then combined the two variables that have strong correlations with sediment yield in a manner consistent with the literature to develop a multi-variable model,

$$Q_s = kA^m S_h^n \qquad (4)$$

where k, m, and n are parameters to be optimized. In this form, the model hypothesizes that a basin's sediment yield is controlled by hillslope gradient and flow at the outlet, with drainage area used as a proxy. We optimize model parameters using non-linear least squares regression (Virtanen et al., 2020). The mean annual sediment yield is estimated from the 1947-2015 DoD in each of the 10 defined watersheds (Section 3.2.1). Watersheds with negative sediment yields (net deposition) are excluded from the model fitting process, as we search for relationships explaining mean annual watershed sediment yield.

4. Results

Table 1. Uncertainty Parameters for all DoDs used in this study.

Name	Start Date	End Date	Mean	RMSE	Range	Sill	90% CI Lower Bound	90% CI Upper Bound
Coleman	9/14/47	9/29/70	1.03	2.83	13.42	6.18	-3.31	5.37
Coleman	9/29/70	10/6/79	-0.67	1.36	9.62	1.14	-2.62	1.29
Coleman	10/6/79	8/21/87	-1.03	2.08	18.93	2.3	-4.01	1.95
Coleman	8/21/87	9/5/90	1.5	2.54	18.43	1.45	-1.88	4.87
Coleman	9/5/90	9/1/15	-0.22	1.11	48.12	1.37	-2.01	1.57
Coleman	9/14/47	9/1/15	0.47	1.95	26.25	2.14	-2.64	3.59
Rainbow	9/14/47	9/29/70	-0.57	1.89	8.9	2.74	-3.54	2.4
Rainbow	9/29/70	8/10/74	-0.33	0.92	15.91	0.69	-1.74	1.09

Rainbow	8/10/74	9/27/77	0.11	0.66	15.74	0.41	-0.96	1.18
Rainbow	9/27/77	9/9/91	0.06	0.6	8.66	0.34	-0.92	1.04
Rainbow	9/9/91	9/1/15	-0.07	0.48	6.86	0.23	-0.86	0.72
Rainbow	9/14/47	9/1/15	-0.78	2.02	7.92	3.12	-3.85	2.28
Mazama	9/14/47	9/29/70	1.12	2.48	29.72	4.21	-2.52	4.76
Mazama	9/29/70	10/6/79	0.09	0.76	22.56	0.45	-1.14	1.32
Mazama	10/6/79	9/18/92	-0.31	1.28	65.27	1.26	-2.35	1.72
Mazama	9/18/92	9/1/15	0.14	1.36	101.91	1.47	-2.08	2.36
Mazama	9/14/47	9/1/15	0.85	2.65	38.17	5.91	-3.28	4.98
Deming	9/14/47	9/29/70	-0.45	1.32	15.02	1.53	-2.49	1.59
Deming	9/29/70	10/6/79	0.54	0.91	2.39	0.14	-0.65	1.74
Deming	10/6/79	9/9/91	-0.03	0.71	23.07	0.43	-1.21	1.14
Deming	9/9/91	9/1/15	-0.18	0.76	26.18	0.47	-1.4	1.03
Deming	9/14/47	9/1/15	0.7	1.34	26.24	1.24	-1.18	2.57
Whole Mountain	9/14/47	9/1/15	0.49	2.25	68.55	3.79	-3.11	4.1

4.1 1947-2015 Overview DEM of Difference Maps

We begin by illustrating changes in glacier position and the locations and magnitudes of different erosion processes within three proglacial valleys where geomorphic activity was more pronounced over the 68 year period between 1947 and 2015.

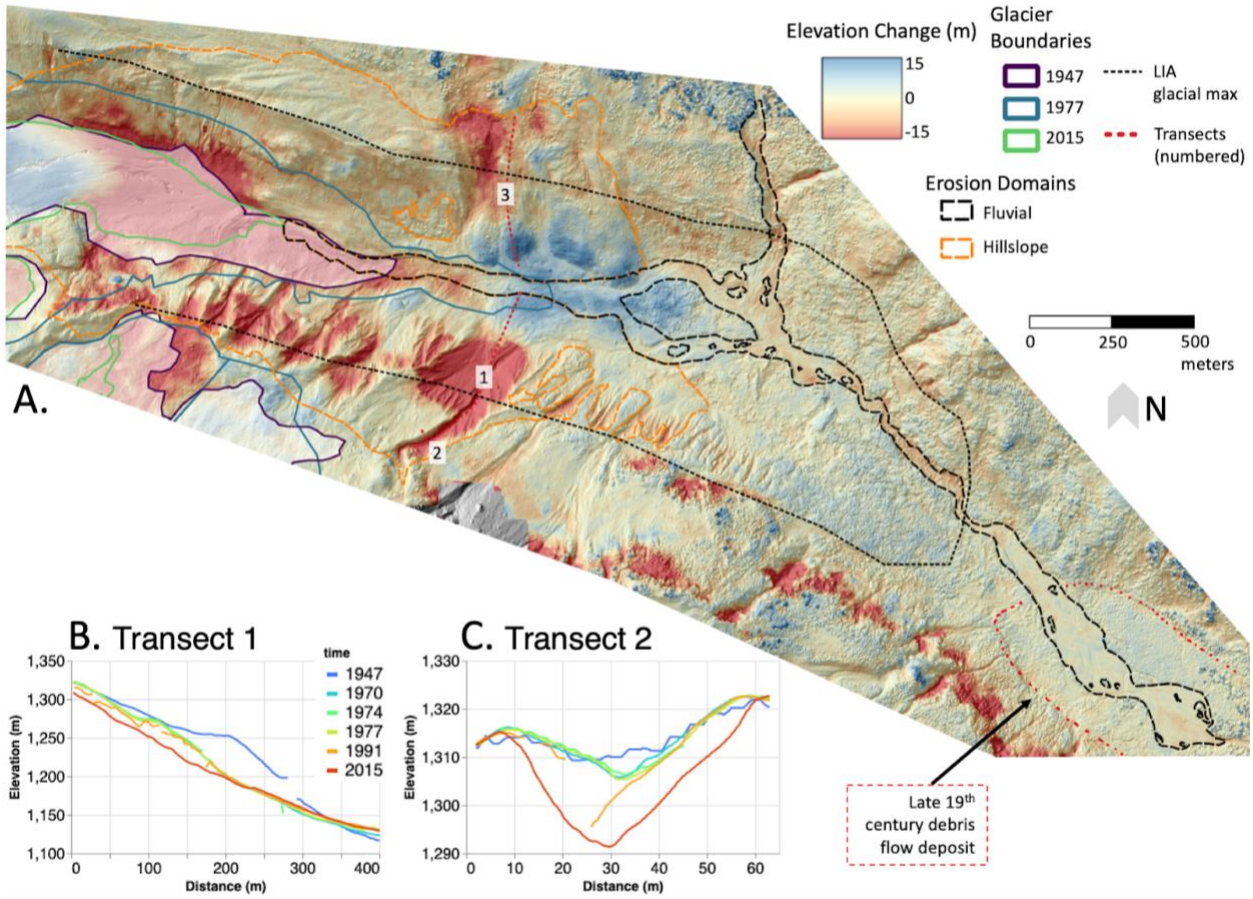

Figure 4. (A) Rainbow glacial valley DoD 1947 - 2015 overlaid on 2015 DEM hillshade. Elevation change color ramp is clamped to -15 and +15 m to bring out detail, though many signals are larger.. Opaque polygons cover elevation changes related to changing glacial extent. The 1977 glacier boundary is shown to indicate where the glacier advanced between 1947 and 1977 and retreated between 1977 and 2015. Glacier-related erosion is visible within the bounds of the 1977

glacier boundary and outside the bounds of the 1947 and 2015 glacier boundaries. The black arrow indicates the footprint of a late 19th century debris flow deposit inferred from LIDAR topography (Fuller, 1980; Hyde and Crandel, 1978). A 1D profile transect for Transect 3 is shown in Figure S2. The profile of Transect 1 in (A) is shown in (B), Transect 2 in (C).

In the Rainbow proglacial basin we observe that most geomorphic change occurred along the LIA lateral moraines (Figure 4A). A number of gullies incised into the north-facing slope of the southern LIA moraine, immediately beneath fluctuating glaciers (Figure 4A and 4C). A single landslide scar is visible on the southern moraine (Transect 1 in Figure 4A and 4B) and the associated deposit is visible in the valley floor beneath the landslide scar (approximately 820,000 m^3 eroded, 713,000 deposited between 1947 and 1970, Table S2). On the northern (south facing) moraine, a rotational slump, which has been active since before 1947 (Fuller, 1980), moved during all periods of measurement and protrudes into the valley floor (Transect 3 in Figure 4A, Figure S2). Some scour of the channel is visible downstream of the landslide deposit and upstream of the LIA glacial max boundary (Figure 4A). Finally, we note that the land surface north of the 1947 and 2015 glacier boundaries and within the 1977 boundary was eroded sometime between 1947 and 2015.

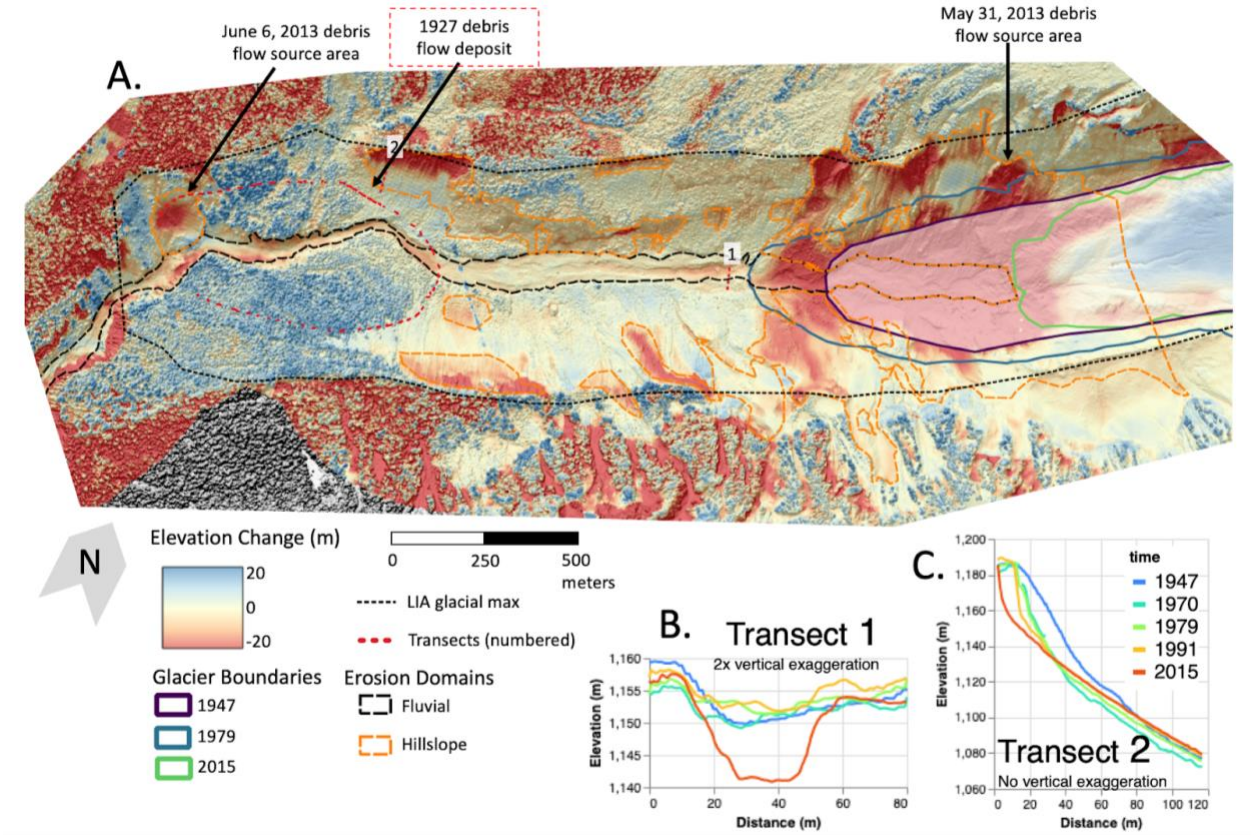

Figure 5. (A) Deming glacial valley DoD 1947 - 2015 overlaid on 2015 DEM hillshade. Elevation changes beyond the range -20 to 20 meters have the same color as changes of -20 and 20 meters. Opaque polygons cover elevation changes related to changing glacial extent. The 1979 glacier boundary is shown to indicate where the glacier advanced (1947 - 1979) and retreated (1979-2015). Glacier-related erosion is visible within the bounds of the 1979 glacier boundary and outside the bounds of the 1947 and 2015 glacier boundaries. (B) 1D cross-sectional transect (see transect 1 in A) shows channel incision by a debris flow observed in 2013. (C) 1D profile transect (see transect 2 in A) showing evolution of an LIA moraine. Source areas for the 2013 debris flows are identified by Tucker et al. (2014). The footprint of the 1927 debris flow deposit is inferred from LIDAR topography and Tucker et al. (2014).

In the Deming proglacial basin, we observe a similar distribution of erosion signals, with most erosion occurring along the tops of LIA moraines. Towards the downstream end of the valley, the tops of LIA moraines have retreated 20 to 40 meters (Transect 2 in Figure 5A and 5C). Other erosion is concentrated near the fluctuating glacial boundaries, where the tops and middle of LIA moraines erode. We identified incised channels by the May 31 and June 6, 2013 debris flows, reported by Tucker et al. (2014), who estimated 100,000 m^3 of material failed during the May 31 event, ran out from 5 up to 9 km downstream and affected turbidity for the length of the Middle Fork Nooksack river. We estimate 70,000 m^3 and 92,000 m^3 of volumetric change for the May 31 and June 6 2013 debris flows events, respectively. Lastly, we note that incision of the stream channel occurs both close to the fluctuating glacier footprint (Transect 1 in Figure 5A and 5B) and approximately 1.5 km downstream, within the 1927 debris flow deposit (Figure 5A).

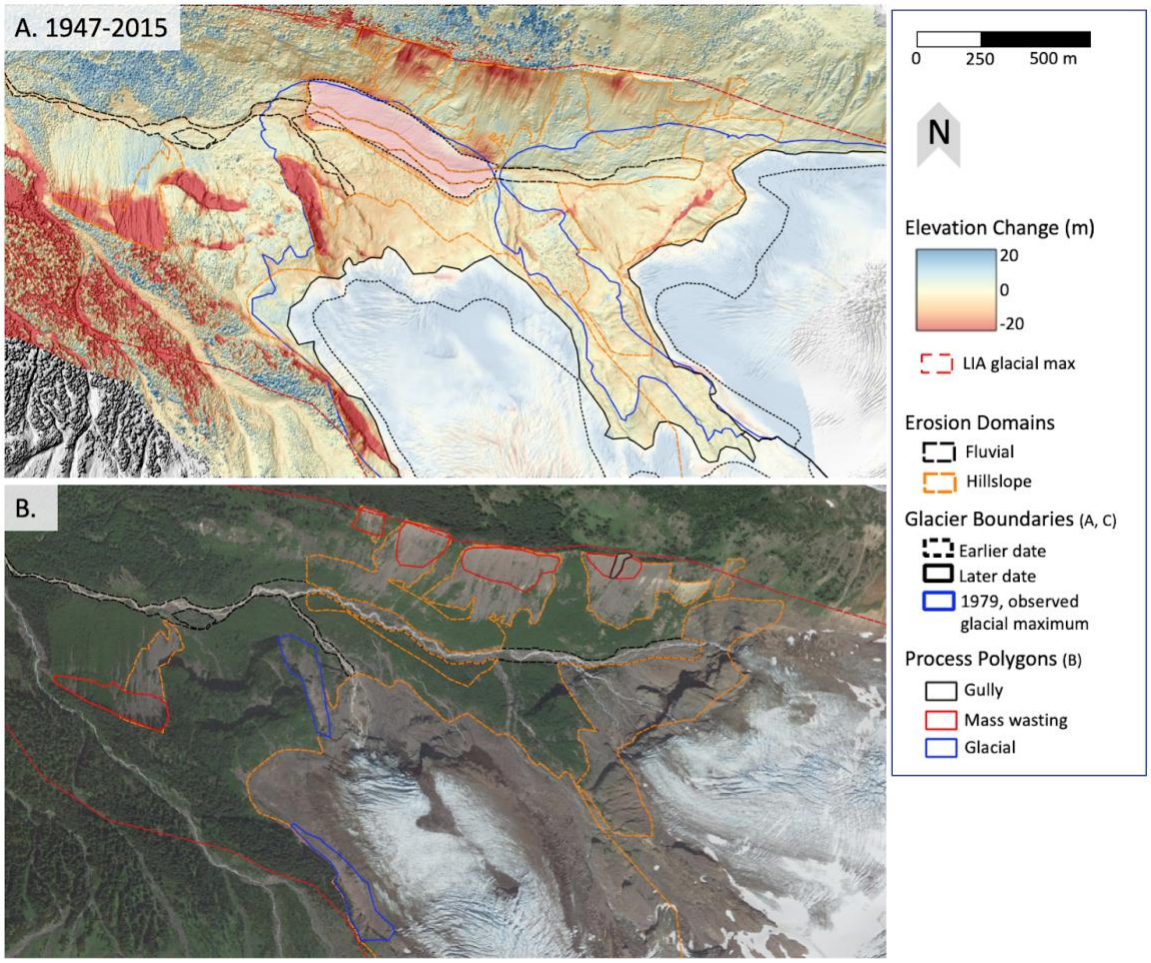

Figure 6. (A and C) Coleman glacial valley DoD for the 1947-2015 interval. The DoD is overlaid on a DEM hillshade from 2015. Elevation changes beyond the range -20 to 20 meters have the same color as changes of -20 and 20 meters. Opaque polygons cover elevation changes related to changing glacial extent. (B) Erosion domains and process polygons overlain on Google satellite basemap (imagery source date 2016-7-28).

In the Coleman proglacial basin, landscape change is isolated to both lateral LIA moraines and a more recently formed moraine within the boundary of the 1979 glacier (Figure 6A). A patch of stagnant ice in the valley floor melted between 1947 and 1970 and obscures any landscape

change in that region during that period. Similar to the downstream end of moraines in Deming basin, erosion of the LIA moraines is characterized by horizontal retreat.

In the Mazama proglacial basin (Figure S4), erosion patterns are similar to those observed in the Deming proglacial basin; erosion is isolated to the tops of LIA moraines and along fluctuating glacier boundaries. We identified both mass wasting and gully sites near Mazama glacier. Minimal changes in the stream channel are observed.

Overall, maps of elevation change between 1947 and 2015 in all four proglacial basins indicate that both relict topography (LIA moraines) and recent glacial fluctuations control erosion rates in proglacial basins. We observe active erosion on steep slopes of LIA moraines. Erosion occurs on the tops of LIA moraines, where glacial fluctuations within our measurement interval appear to have no influence. Erosion in the middle of LIA moraine walls appears to be associated with advance and retreat of glaciers during our measurement time interval. Lateral, uniform retreat of the tops of LIA moraines is observed in Deming and Coleman valleys and, while the mechanism associated with this erosion process is not clear from the remotely-sensed data presented here, field observations indicate that dry ravel is a likely explanation (Figure S7)

4.2 Sediment yields of proglacial basins (1947-2015)

In this section we compare the total yield observed in each proglacial basin in relation to terrain characteristics (Table 2).

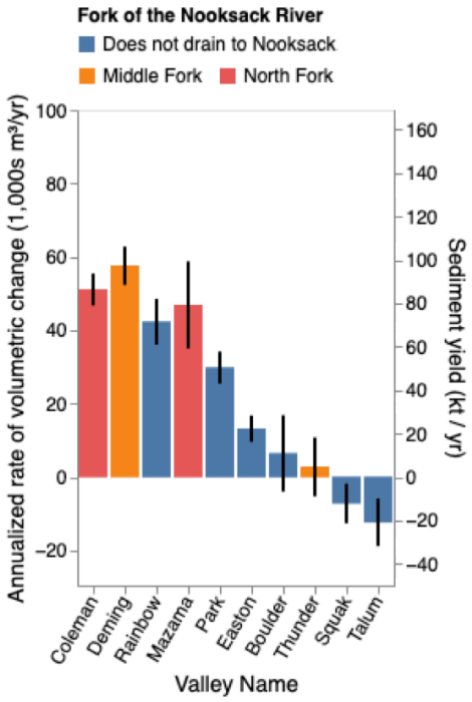

Figure 7. Annualized volumetric change and sediment yield for 3 time intervals in all measured proglacial watersheds. Sediment yields are calculated by converting volumetric change measurements with a porosity of 0.35 and rock density of 2600 kg/m^3. Watersheds with negative values are net depositional. *All watersheds use the 1979 DEM except for Rainbow and Park, which use the 1977 DEM.

Sediment yields vary significantly across basins on Mount Baker with net sediment yields as high as 97.26 ± 8.82 kilotonnes per year (Deming basin) and net deposition as high as 20.90 ± 11.0 kilotonnes per year (Talum basin) (Figure 7). Most of the measured erosion on Mount Baker occurs in five valleys (Coleman, Deming, Rainbow, Mazama, and Park basins), with Easton contributing a smaller amount of geomorphic change. In two basins (Boulder and Thunder), our measured rates of change are indistinguishable from zero. In another two basins (Squak and Talum), geomorphic change rates are negative, indicating net deposition. This deposition may be attributable to deposition of material associated with formation of moraines, for which the source areas are obscured by ice. Small but widespread positive elevation signals contributed by sparse tree growth may also be responsible for these net depositional measurements. Regardless, we interpret the net depositional basins as basins within which there was negligible net erosion.

Table 2. Terrain and watershed characteristics for each proglacial zone. Depositional Squak and Talum proglacial basins are shown in lighter grey font to indicate their exclusion from the model fitting.

Glacier	A Watershed Drainage area (km^2)	S_c Longitudinal channel slope (degrees)	S_h Mean slope of hillslope domain (degrees)	ΔA_g Glacial retreat area (km^2)	Sediment Yield (tonne/ yr)	Sediment Yield Normalized (tonne/ km^2/yr)	Sediment Yield Uncertainty (tonne/yr)
Park	9.9	5.5	28.9	0.390	50,359	5,062	7,401
Rainbow	12.9	5.0	30.5	0.687	71,494	5,561	10,554
Boulder	5.6	10.8	24.6	0.802	10,853	1,926	17,595
Thunder	7.1	11.6	22.6	0.180	4,639	652	13,554
Easton	4.7	9.8	25.3	0.185	22,240	4,733	6,069
Deming	11.6	6.8	35.9	0.369	97,263	8,393	8,818
Coleman	13.9	7.2	30.9	0.658	86,319	6,230	7,367
Mazama	13.2	7.7	40.3	0.563	79,229	6,004	20,080
Talum	3.13	16.5	26.0	0.982	-20899	-6677	10,975
Squak	3.95	12.4	27.2	0.750	-12,215	-3094	9126

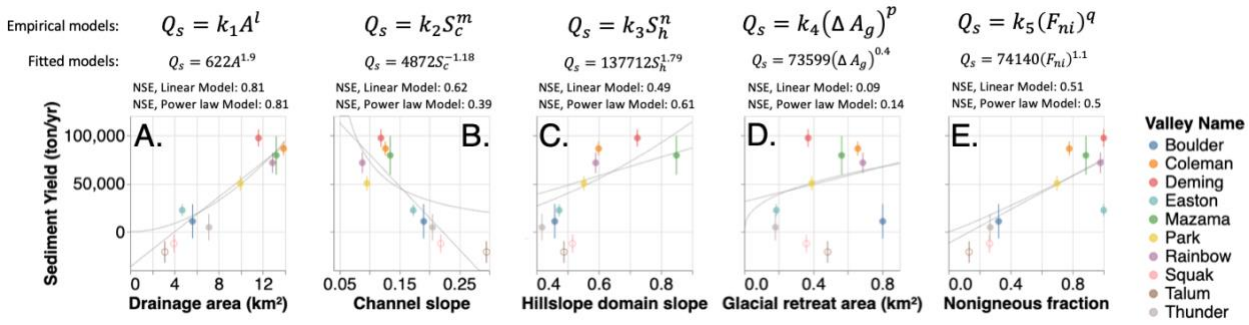

Figure 8. Relationships between terrain characteristics and mean annual sediment yields in erosional valleys of Mount Baker calculated for the 1947-2015 period (Table 2, Figure 7). Open circles represent net depositional valleys, not included in curve fits. Uncertainty for each sediment yield measurement is represented by vertical bars and values are presented in Table S4. Lines plot fitted linear and power functions. Commonly used power functions in the literature, and their estimated parameters are shown above each panel. Nash-Sutcliffe model efficiency (NSE) values are shown above each panel. For the fitted lines (linear models), NSE may be interpreted similarly to r^2.

Figure 8 shows how sediment yield rates are correlated with topographic characteristics, glacial retreat, and lithology. Sediment yield is strongly positively correlated with drainage area, hillslope domain slope, and nonigneous fraction (r^2 values of 0.81, 0.49, and 0.51, respectively, NSE (Linear model) values in Figure 8 are equivalent to r^2). Our measurements of nonigneous fraction indicate that the 10 basins on Mount Baker can be categorized into two groups, those underlain by igneous rocks (mostly andesitic lava flows, Tabor et al., 2003) and those underlain by marine sedimentary rocks and talus/glaciogenic deposits (Figure 8E, S3). The four basins with igneous-dominant lithologies all have either negative sediment yields (net depositional, Talum and Squak basins) or sediment yields that are indistinguishable from zero within uncertainty (Boulder and Thunder basins, Figure 8E). When we fit the same models only to basins with nonigneous fractions larger than 0.5, the predictive power of nonigneous fraction disappears entirely (r^2 of 0.0, Figure S9) and the predictive power of glacial retreat area increases considerably (r^2 of 0.4, Figure S9). Thus, we did not include rock type in further analysis. Sediment yield is negatively correlated with channel slope (r^2 of 0.62), implying that basins with steeper channel slopes do not yield more sediment.

It is worth noting that although the two net-depositional basins were not included in the model fitting process, the net depositional basins continue most trends exhibited by the other 8 basins. The two net depositional basins drain the smallest areas of all basins (Figure 8A), have the steepest channel slopes (Figure 8B), have relatively low hillslope domain slopes (Figure 8C) and have the greatest proportion of underlying igneous lithology (Figure 8E).

The performance of the two GTLs based on drainage area and hillslope domain slope (Figure 8A and 8C, NSE of 0.81 and 0.61, respectively) indicates these two variables are the strongest predictors of sediment yield when considering the eight net erosional basins. The performance of these models led us to attempt to fit a model inspired by the GTL literature (Section 3.6, equation 4). The fitted power law model incorporating drainage area and hillslope domain slope (Figure 9, equation 4) performs well with a NSE of 0.84. This is only a slight improvement from the performance of the power law model incorporating only drainage area (NSE of 0.81, Figure 8A). Including other variables, such as glacier area, in power-law forms did not provide any further improvement in model performance.

$$Q_s = kA^l S_h^n$$

$$Q_s = 1764A^{1.58}S_h^{0.56}$$

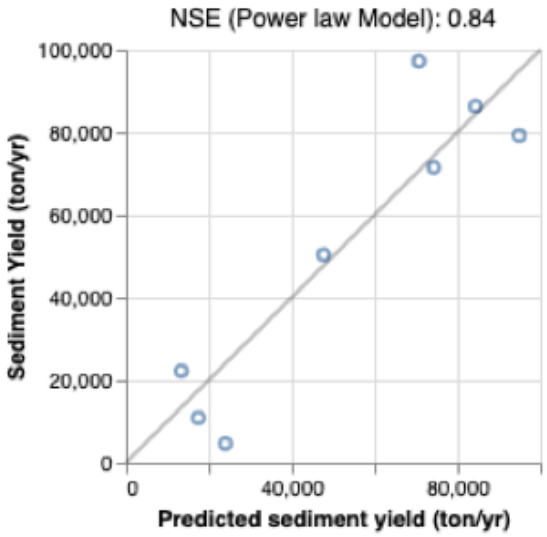

Figure 9. Measured sediment yield versus the predicted sediment yield for the area and hillside slope model (Equation 4). The generic power-law form and fitted parameters are given in the figure.

4.3 DEM of Difference Time Series Maps and Time Series Measurements of Geomorphic Change

We address the research questions 1 and 4 (Section 1) by examining DoD time series to see how rates of geomorphic change evolve over time. We present DoD time series maps in Rainbow (Figure 10) and Deming (Figure 11) proglacial basins as they were two of the most active valleys during the study period (Mazama DoD time series shown in Figure S4). We then present time series measurements of gross erosion and deposition and cumulative volumetric change in all four high erosion sites to demonstrate how temporal variability in geomorphic change rates are consistent across different basins.

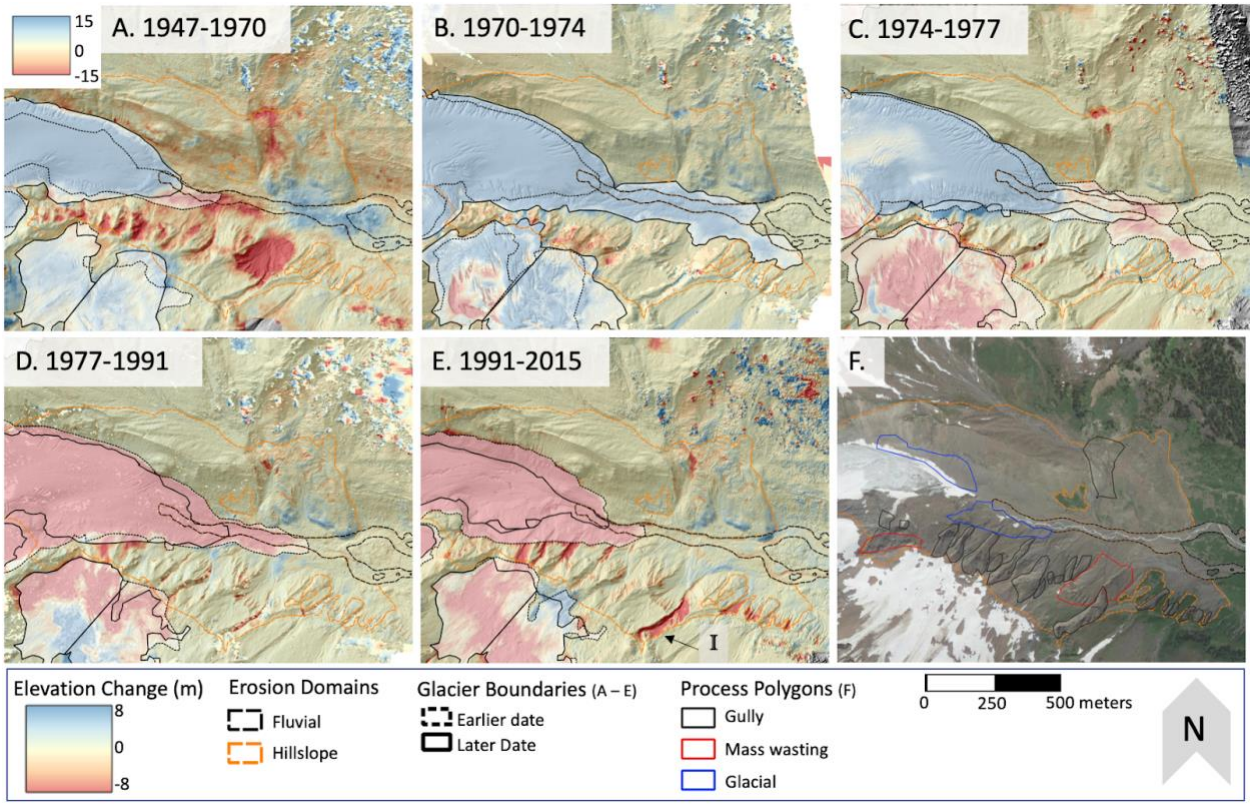

Figure 10. (A - E) Rainbow glacial valley DoDs shown for 5 time intervals, DoDs are overlaid on DEM hillshades from the later date. Except for (A) elevation changes beyond the range -8 to 8 meters have the same color as the limit colors. Opaque polygons cover elevation changes related to changing glacial extent. Panel (A) has a different color scale, shown inset in the panel. (F) Erosion domains and process polygons overlain on Google satellite basemap (imagery source date 2016-7-28). Extents of all panels show the upstream/near-glacier portion of the area shown in Figure 4. Roman numerals indicate features discussed in text.

DoD time series in the Rainbow glacier basin indicate that the occurrence of erosion events is variable in time (Figure 10). The earliest time period was the most geomorphically active; the aforementioned 820,000 m^3 landslide occurred during the first measurement interval. Gully erosion is concentrated primarily in the first (1947-1970) and last (1991-2015) measurement intervals. We also observe that erosion of gullies propagates upstream with time (feature I in Figure 10E). Between 1970 and 1974, a large slug of material flowed from gullies on the southern moraine and deposited in the valley floor. Imagery indicates this material is mostly ice and snow, and ablation signals in the following intervals confirm this interpretation (Figure S5). We include the area of this deposit and subsequent melt within the glacier boundaries to remove the ice and snow related elevation changes from our measurements.

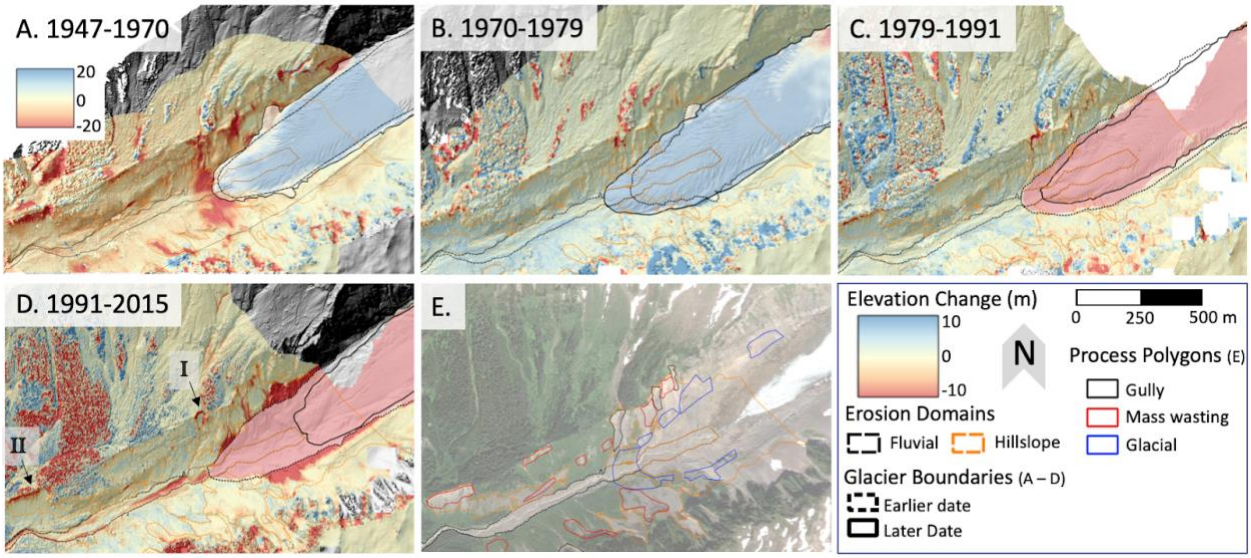

Figure 11. (A - D) Deming glacial valley DoDs shown for four time intervals, DoDs are overlaid on DEM hillshades from the later date. Elevation changes beyond the range -10 to 10 meters have the same color as changes of -10 and 10 meters. Opaque polygons cover elevation changes related to changing glacial extent. Panel (A) has a different color scale, shown inset in the panel. (E) Erosion domains and process polygons overlain on Google satellite basemap (imagery source date 2016-7-28). Extents of all panels show the upstream/near-glacier portion of the area shown in Figure 6. Roman numerals indicate features discussed in text.

DoD time series in the Deming glacier basin exhibit similar temporal patterns (Figure 11). Hillslope erosion is mostly isolated to the first and last measurement periods; erosion rates between 1970 and 1979 are nearly indistinguishable from zero (Figure 12). Persistent erosion of a gully north of the glacier terminus is observable in all time periods (Figure 11D, I). This gully also exhibits some upstream propagating behavior, with erosion occurring along the length of the gully between 1947 and 1970, closer to the top between 1970 and 1991, and isolated to the very top of the LIA moraine between 1991 and 2015 (Figure 11). Historical and modern imagery indicate that an ephemeral stream exists in this gully. Persistent slope failure of moraine tops at the downvalley end of the study area (i.e. Transect 2, Figure 5A; Figure 5C) is observed across all measurement periods (Figure 11D, II).

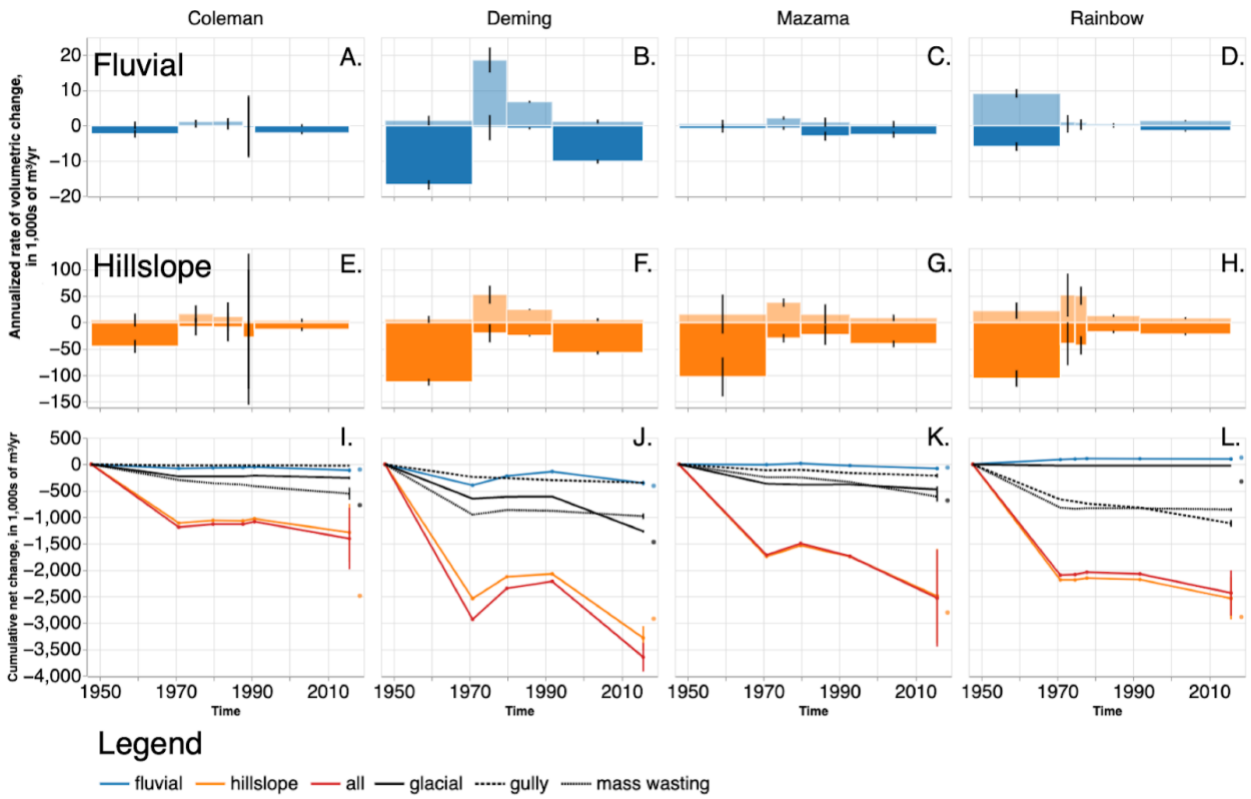

Figure 12. Gross volumetric change measured in fluvial (A - D) and hillslope (E - H) domains for the four high erosion sites; erosion is negative, deposition is positive. (I - L) Cumulative net volumetric change in the four high erosion sites attributable to the fluvial and hillslope domains and as well as process categories. "All" is the combined cumulative change in the fluvial and hillslope domains. Circles on the far right indicate the volumetric change measured with the 1947-2015 DoD in the fluvial domain (blue), hillslope domain (orange), and in the glacial process areas (black). Note that measured glacial erosion is generally larger using the 1947-2015 measurement because land area over which glaciers advanced and then receded is only measurable using the 1947-2015 DoD.

Time-series measurements of gross positive and negative volumetric change and cumulative net volumetric change are presented for the four high erosion sites in Figure 12. In all four high erosion sites, the change measured prior to 1970 contributed the majority of cumulative net volumetric change (Figure 12 I - L) and gross hillslope erosion was greatest during the same period, Figure 12 E - H). Hillslope erosion rates were generally lower between 1970 and 1990 and increased after 1990 in Deming and Mazama proglacial zones (Figure 12 E - H). Significant deposition is observed only between 1970 and 1991 in Deming basin (Figure 12B and 12F), between 1970 and 1979 in Mazama basin (Figure 12C and 12G, and in all periods in Rainbow basin (Figure 12D and 12H). Gully erosion rates are consistently erosional in Deming, Mazama, and Rainbow basins, although gully erosion slowed or ceased during the 70s and 80s (negative slope of gully lines, Figure 12 I - L). Similarly, mass wasting rates are consistently erosional in Coleman and Mazama basins aside from slow-downs during the 70s and 80s (negative slope of mass wasting lines, Figure 12 I - L).

In Rainbow and Deming basins, mass wasting processes erode significantly more material during the first measurement period than afterwards (Figure 12J and 12L). In Rainbow basin, this mass wasting erosion is attributable to the aforementioned landslide (between 1947 and 1970), the deposit of which persists in the valley floor. In Deming basin, mass wasting (retreat) of LIA

moraine tops appears in all time interval DoDs (Figure 11), but our volumetric measurements indicate that this retreat actually contributed very little net erosion except during the initial measurement period (Figure 12J).

5. Discussion

5.1 Spatial Variability of Erosion

5.1.1 Intra-watershed

Paraglacial adjustment, the relaxation of relict LIA moraines, is the dominant behavior observed in our maps of proglacial landscape change. Analysis in four high erosion sites (Section 4.1) reveal that most observed erosion is removing material from LIA moraines. This observation is consistent with the idealized description of proglacial erosion presented by Carrivick and Heckmann (2017), who state that the majority of geomorphic activity in glacierized landscapes occurs within the bounds of LIA moraines. We confirm this to be true on Mount Baker, with the notable addition that erosion processes often erode through LIA moraines, connecting the landscape on either side of the moraine crest, initiating erosion and increasing erosion rates outside and above LIA bounds (e.g. feature I in Figure 10E, Mancini and Lane, 2020).

Much of the LIA moraine erosion appears unrelated to post-1947 glacial fluctuations (advance 1947-1979, retreat thereafter). In the Rainbow basin, a nearly 1 million cubic meter landslide removed a distinctive profile with slope-break formed by the LIA moraine (Figure 4b). We also observed an even larger mass of land, a slow-moving earthflow, deforming the northern moraine. In Deming, Mazama, and Rainbow basins, gullies appear on and chunks of land fall from moraine crests, far from the fluctuating glacier boundaries we observe in our dataset. In Deming and Coleman basins, wide swaths of moraine crests retreat by mass wasting. In the case of the northern Deming LIA moraine, this process progressively leads to the steepening of moraine slopes (Figure 5C). This style of erosion seems isolated to areas where dense forest grows to the edge of the LIA moraines, likely resisting the erosion of the top of the moraine.

Erosion processes related to post-1947 glacial fluctuations also act to erode LIA moraines. In the Deming basin, significant land surface lowering is observed within the footprint of the 1979 glacier (the maximum observed glacier footprint). Notably, the source area of the May 31, 2013 debris flow identified by Tucker et al. (2014) is partially contained within the 1979 glacier boundary (Figure 6A), indicating that the failure that initiated the debris flow was associated with post-1979 glacial recession, as Tucker et al. hypothesize. In the Rainbow basin, the 1947-2015 DoD (Figure 4A) reveals significant land surface changes within the footprint of the 1977 glacier (the maximum observed glacier footprint) but outside the footprints of the 1947 and 2015 glaciers. While the processes that cause this lowering are not immediately obvious, Tucker et al.'s observations in Deming basin indicate that debuttressing and subsequent mass failure is a likely explanation.

To compare the role of the three erosion processes, glacial erosion, gully erosion, and mass wasting; we sum the net cumulative erosion attributable to each process measured using the 1947-2015 DoD (Figure 12) across all four high erosion basins. We find that the total volumetric erosion attributable to the three process categories is approximately equal within an order of

magnitude. Glacial erosion contributes 40.6% (3.25 million m^3), gully erosion 21.9% (1.75 million m^3), and mass wasting erosion 37.5% (3.00 million m^3) to the total sediment yield. Erosion categorized as "glacial" due to its apparent relationship with post-1947 glacial fluctuations is nearly as large as "gully" and "mass wasting" erosion, which are classified erosion sites where post-1947 glacial fluctuations do not appear to have an impact. This result indicates that in the absence of future glacial fluctuations, total volumetric erosion rates will likely change less than one order of magnitude. Overall erosion rates may decrease, as we measured 40.6% of all erosion is related to glacial fluctuations during our measurement time period, but erosion of large unstable, LIA relict landforms is likely to continue at similar rates.

It is worth noting that our classification methodology is unable to capture erosion that occurred due to pre-1947 glacial fluctuations. Rapid glacial retreat between 1930 and 1945 (Dick, 2013) may be responsible for rendering portions of the landscape unstable, and these areas may be responsible for erosion sites that we do not classify as "glacial".

5.1.2 Inter-watershed

Sediment yields measured in the 10 Mount Baker basins vary significantly (Figure 7). When considering only the most erosive basins, however, yields are remarkably similar. Yield in Coleman, Deming, Rainbow, Mazama, and Park basins vary by little more than a factor of two (Figure 7). Differences among the eight net erosional basins may be explained by a number of factors. The primary controlling factor appears to be lithology; an analysis of a bedrock geologic map reveals that basins with low sediment yields (Boulder and Thunder basins, Figure 8) as well as the two net depositional valleys that are excluded from the correlations (Squak and Talum) are underlain by igneous bedrock (andesitic lava flow) (Figure S3). The relatively low yield of the Thunder basin can also be explained by this bedrock.

The apparent explanatory power of the nonigneous fraction variable indicates that the topography and lithology of Mount Baker and its history of eruption and edifice construction are important factors in determining the sediment yields of different basins. Determining whether topography causes erosion or whether erosion and topography share a causal variable is difficult.

The basins on Mt Baker fall into two groups: basins with high and low sediment yields, with at least a factor of two difference in sediment export between them. Basins with high sediment yields (Mazama, Coleman, Deming, Rainbow, Park basins) have relatively narrow, deep, confined proglacial zones, with long glacial "tongues" that feed into U-shaped valleys with low-gradient valley floors. Basins with low sediment yields are underlain mostly by igneous, andesitic lava flows, have less confined proglacial zones and steep channels, and are mostly on the southeast side of Mount Baker. To better understand the reasons for this duality, we examined the interactions of the predictive variables presented in Figure 8 and found that nonigneous fraction positively predicts drainage area and hillslope domain slope and negatively predicts channel slope; no obvious relationship exists between nonigneous fraction and glacial retreat area (Figure S8). These interactions may explain why channel slope is negatively correlated with sediment yield. Channel slopes are steeper while hillslope domain slopes are shallower in low-sediment-yielding basins underlain by igneous bedrock. We hypothesize that as the glaciers retreated and exposed proglacial landscape, lower weathering and erosion potential of igneous rocks could have limited channel incisions and the development of hillslopes through

the widening of LIA moraines. While in basins with nonigneous rocks, more rapid removal of proglacial debris and carving of channels could have gradually reduced channel slopes, while at the same time leading to the development of steeper slopes on the sides of the moraines as a result of base level fall due to channel incision. The apparently strong positive relationship between nonigneous fraction and drainage area (with the Easton basin as an outlier to this relationship) and the positive relationship between igneous fraction and hillslope domain slope (Figure S8) also points to the importance of volcanic history and pre-existing topography in determining basin-wide sediment yields.

To the best of our knowledge, our results present the first application of simple watershed-scale sediment yield equations to upland, glacierized basins over modern observational time scales. While geomorphic transport laws generally rely on channel slope and drainage area as proxies for critical shear stress and stream power, we found inverse correlations between sediment yield and channel slope. Our observations show that minimal erosion of and deposition in stream channels accompanies significant erosion of hillslopes (Figure 8B). As a result, we find that channel slope is a poor predictor of sediment yield. Instead, drainage area at the outlet and spatially averaged hillslope gradients appear to be the dominant controls on sediment yield from proglacial basins. These variables are combined in a power-law model: $Q_s=A^{1.58}S_h^{0.56}$ (NSE=0.84). Our empirical formulations (Figure 8) are far from being models that can be used to predict future changes in glaciated landscapes, but we find them to facilitate our understanding of both the dominant erosion processes and the impact of volcanic and geological history on basin-scale landscape evolution.

Our findings suggest that hillslope erosion events frequently initiate debris flows and flow out of the basin, bypassing and sometimes scouring the stream channels. Tucker et al. (2014) identified this type of behavior in Deming basin. Although the two debris flows discussed by Tucker et al., account for just 15% of the total sediment yield of Deming basin (see Section 5.2.2), they also suspect that two similar events occurred in 2003 and 2008. Additional debris flow events in Deming and other basins almost certainly occurred during our measurement period. However identification of which gully and mass-wasting sites (in Figure 5 and 11) failed and initiated debris flows would be speculative at this point. The hypothesis that debris flow events dominate sediment export from proglacial basins is supported by the fact that nearly all of the gully and mass-wasting sites identified on Mount Baker in this study are on slopes greater than 34 degrees, the minimum slope required for debris flow initiation with minimal shear stress identified experimentally by Prancevic et al. (2014).

While we did not attempt to quantify climate-related reasons for inter-basin erosion rate variability, we did examine 800-meter gridded average annual precipitation (1981 - 2010) reanalysis data (PRISM Climate Group) and found that at this coarse scale, precipitation rates do not correlate with basin sediment yields.

5.2 Role of Proglacial Sediments at the River Basin Scale

5.2.1 Nooksack River Measurements

Table 3. Literature review and reanalysis of sediment yields in the North and Middle forks of the Nooksack River system. We use suspended sediment load measurements in each fork (Anderson et al., 2019) to infer a range of bedload measurements (using the results of Turowski et al., 2010) and, combining these measurements, estimate annual sediment

flux. We then examine what percentage of this flux could be attributable proglacial erosion (using measurements from this study) and bluff/terrace erosion (using reanalysis of measurements from Scott and Collins, 2021). Detailed account of calculations used to produce this table provided in Table S5.

	Suspended Sediment Load	Total Load	Bluff/terrace erosion		Proglacial erosion			
Source:	Anderson et al., 2019	Anderson et al., 2019 & Turowski et al., 2010	Scott and Collins, 2021		This study			
Measurement time period:	2014 - 2016	2014-2016[1]	2005 - 2017[2]		1990 - 2015[3]		1947 - 2015	
Units:	kilotonnes / year	kilotonnes / year	kilotonnes / year	percent of total load[4]	kilotonnes / year	percent of total load[4]	kilotonnes / year	percent of total load[4]
North Fork Nooksack	220-260	232 - 578	0	0	58	18% (10 - 26%)	79	24% (13 - 35%)
Middle Fork Nooksack	190-240	200 - 600	0	0	104	36% (17 - 54%)	102	35% (17 - 53%)
North and Middle Forks[3]	590-605	621 - 1100	74	10% (7 -12%)	180	23% (16 - 30%)	267	40% (24 - 56%)

1. Anderson et al. (2019) present suspended sediment load measurements for the water years 2014-2016 and for water year 2016, lower and upper bounds are selected from the combined measurements.
2. Bluff measurements are taken from 3 LIDAR DEMs of difference with dates 2005 - 2015, 2005 - 2017, 2006 - 2017
3. Measurements for each fork are using the latest DOD measurement time interval available for each basin. North Fork (Mazama basin) is 1992-2015, Middle Fork (Deming and Thunder basins) are presented as a single value and range, where the range represents the upper and lower bounds of total load estimates and the single value is the mean.
4. Combined north and middle fork suspended load estimates are calculated from Anderson et al., 2019, using the main stem measurements minus contributions from the South Fork.

Here we compare our total load estimates to previously published sediment load estimates in the Nooksack River system to approximate the amount of sediment contribution by proglacial basins. This comparison is of particular interest in the Nooksack River, which has a history of significant aggradation and managed dredging operations and, recently, has been the site of catastrophic flooding which may be due in part to changes in channel conveyance (Ahrendt et al., 2022). A common adage regarding river systems in Western Washington is that glacierized volcanoes are constantly shedding sediments and filling rivers. To test this hypothesis, we develop a sediment budget for the Nooksack River using measurements of stream bank terrace erosion (Scott and Collins, 2021) and suspended sediment load measurements in the three forks (North, Middle, South) and the main stem of the Nooksack river (Anderson et al., 2019). Mazama basin feeds the North Fork and Deming and Thunder basins feed the Middle Fork Nooksack River. Mazama, Coleman, Deming, and Thunder all feed the main stem Nooksack River (Table S5). To estimate total load, we use the results of Turowski et al. (2015) to infer a range of bedload rates for each suspended load measurement reported by Anderson et al. (2019). Our estimates of sediment yield represent a minimum estimate of the total load exported from proglacial basins (Section 3.3.3). The calculations used to create the sediment budget are presented in Table S5.

Considering the range of measurements and the full range of estimated total loads (Table 3), proglacial sediments measured in our study may account for as little as 10% (North Fork gage, 1992-2015 DoD interval) or as much as 56% (combined North and Middle Fork gages, 1947-2015 DoD interval) of total load. The upper end estimates of proglacial and terrace erosion

contributions to total load (56% and 12%, respectively) account for a combined 68% of the total load.

Czuba et al. (2012) note that sediment yields of glacierized stratovolcano basins are an order of magnitude larger than the yields of forested catchments subject to human intervention based on measurements of sedimentation in Alder lake near Mount Rainier. There is 32% of total load not explained by our combined upper end estimates of proglacial and terrace erosion, 68%. The sediment unaccounted for may be from forested catchments around Mount Baker that contribute more sediment than those near Mount Rainier or from other major erosional processes that we are not accounting for. It is also possible that Mount Rainier is eroding at a faster rate than Mount Baker or that the bluff and terrace erosion and proglacial yield estimates presented in Table 3 are underestimates. Attrition of proglacial sediments as they move from uplands to the sections of river where the suspended load measurements are taken may mean that we overestimate proglacial contribution to total load.

Overall, we observe that proglacial sediments could make up a significant portion of riverine sediments in the Nooksack river, particularly in the Middle Fork. Contributions by proglacial basins almost certainly exceed contributions by stream terrace erosion in the main stem (180-267 ktons/y contributed by proglacial basins, 74 ktons/y contributed by stream terrace erosion, Table 3). Actual sediment yields of proglacial basins are also almost certainly larger than those calculated in our study. Our measurements over Mount Baker were significantly limited by the coverage of historical DEMs and we can easily observe significant erosion uphill and outside of our limited measurement area on the southeast side of Deming Valley, which were excluded to lack of repeat DEM availability. Additionally, our methods do not account for any subglacially sourced sediment, which may form a significant portion of the suspended load leaving proglacial basins.

5.2.2 The Debris flow record

Table 4. Literature review of debris flows on Mount Baker

Source	Volume (1,000's of cubic meters)	Runout distance (km)	Basin	Date	Notes
Tucker et al (2014) and Fuller (1980)	10,000	9.5 - 12	Deming	June 1927	
Tucker et al (2014)	100	5.6 - 8.8	Deming	May 31 2013	
Tucker et al (2014)	N/A	N/A	Deming	June 6 2013	
Tucker et al (2014)	N/A	> 4	Deming	October 2003	Destroyed footbridge at Ridley Creek trail crossing 4km downstream of 2013 glacier terminus.
Hyde and Crandel (1978)	13,000	9km	Rainbow	Late 1800s	Same events described by Fuller (1980).
Fuller (1980)	N/A	N/A	Rainbow	Early 1860s	Fuller identifies that the deposit noted by Hyde and Crandel is actually the result of two separate events.
Fuller (1980)	N/A	N/A	Rainbow	1888	

To investigate the relative contribution of debris flows to estimated sediment yields and the role of debris flows in shaping the proglacier zones we compare our estimates of volumetric erosion rates on Mount Baker to debris flow events on Mount Baker reported in the literature (Table 4). Tucker et al. (2014) and Fuller (1980) both discuss late 19th century debris flows in Rainbow basin, which only appear in our dataset as relict topography (Figure 4A). Scars left by recent debris flows in Deming basin (Tucker et al.) are visible in our dataset (Figure 5A). Tucker et al. report two debris flows in the spring of 2013. One is estimated to have carried 100,000 m^3 of material; no estimate for the second debris flow was reported (Table 4). Our estimates of volumetric change for these two events are 70,000 and 92,000 cubic meters for the May 31 and June 6 events, respectively. Conservatively assuming Tucker's larger estimate of 100,000 m^3 applies to both events, these two events account for approximately 15% of the gross hillslope erosion measured during the 1991-2015 measurement period (57,500 +/- 2,700 cubic meters per year, Table S2). The source area of the May 31 event is adjacent to and across the valley from other similar appearing erosional scars. Tucker et al. (2014) observed that deposits from the 2013 events partially eroded within weeks and predicted that smaller debris flow deposits may be entirely eroded within a few years. These observations together indicate that additional, unrecorded debris flows have likely occurred in Deming basin and elsewhere these events may account for a substantial portion of the sediment export. Debris flows as the primary mechanism of hillslope erosion may also explain why we observe significant hillslope erosion with minimal deposition in the valley floor - material frequently leaves hillslopes as debris flows and bypasses the within-LIA-bounds stream channel entirely (Section 5.1.2).

Tucker et al. (2014) and Fuller (1980) both discuss a June 1927 debris flow event and each estimate a travel distance of 12 km and 9.5km downstream, moving ~10 million m^3 of sediment. Some of the deposit associated with this event is still visible in the Deming proglacial zone and one of the two 2013 debris flows initiated on a hillslope formed on this deposit (Figure 5A). This massive event, along with those recorded as originating near the Rainbow proglacial zone (Table 4), indicate that intermittent (occurring perhaps less than once per century) debris flow events may have large implications for local proglacial geomorphology and may create unstable topography that can later fail, instigating additional debris flow events. Notably, the total net cumulative volumetric change measured in the Deming proglacial zone between 1947-2015 was 3.65 +/- 0.269 10^6 m^3, approximately one third of the volume moved during the 1927 event. Though measured events since the 1927 event are much smaller, recent debris flows still go undetected and cause damage. Tucker et al. describes an event in October 2003 of unknown size (Table 4) destroyed a footbridge on a trail 4 km downstream of the 2013 glacier terminus. Evidence in Deming basin indicates that across Mount Baker, debris flows may be a primary mechanism of erosion and sediment export in proglacial basins.

5.3 Temporal Variability of Erosion - Three Competing Influences

Our 68 year record of landscape change begins approximately a century after the end of the LIA (Dick, 2013; Harper, 1993), and captures proglacial landscapes, where most geomorphic change on Mount Baker is concentrated. At the onset of a paraglacial period, erosion rates are expected to be high and to decay thereafter, as unstable landforms are broken down (Carrivick and Heckmann, 2017). Assuming deglaciation continues into the future, we may expect erosion rates and sediment yields to decrease as glaciers disappear and relict landforms smooth. Superimposed

on this decay in erosion rates, over shorter, decadal timescales, are glacial and climate fluctuations. Decadal climate fluctuations instigate glacial advance and retreat and our results demonstrate that these glacial movements contribute to increased erosion rates (Section 5.1.1). The same climate fluctuations may also exert more direct control on erosion rates by modifying precipitation rates and intensities and the resulting magnitude of shear stresses exerted on the land surface. Our record allows us to explore the competing influences of three drivers of erosion in proglacial landscapes: (1) paraglacial adjustment of relict landforms, (2) short term glacial fluctuations, and (3) climate.

Long-term adjustment from the unstable landforms created during the LIA is the dominant, first order erosional behavior (5.1.2), which inherently produced the initial topographic states, as represented in DEMs, for erosion processes to manifest on. Erosion associated with the decadal glacial fluctuations observed during our study period appears to act as a secondary control. We observe a significant amount of erosion of land surface where glaciers advanced and retreated, covering and then uncovering bareground areas. In the Deming and Coleman basins, approximately half of all erosion is glacial erosion and in Mazama and Rainbow basins, one fifth is glacial-driven erosion (according to our classification scheme, Figure 12). Across all four high erosion sites, erosion related to post-1947 glacial fluctuations accounts for 40.6% of erosion in identified erosion sites.

Identifying the direct impact of climate fluctuations via precipitation on our measurements is challenging due to the limited temporal frequency of the DEM dataset. Even so, our measurements of volumetric erosion rates separated by process suggest that climate directly influences erosion rates. Our measurement period lasts one full oscillation of the Pacific Decadal Oscillation (PDO); an analysis of climate data presented by Anderson and Konrad (2019) indicates that the PDO resulted in cooler-wetter weather between the mid 1940s and late 1970s, warmer-drier weather between the late 1970s and early 2000s, and cooler-wetter weather again starting sometime around the year 2000. Anderson and Konrad also show a rapid increase in the upper range of fall rain storm intensity occurring around 1990 and argue that this may be responsible for increased sediment delivery in recent decades.

The colder-wetter period of the 1940s-1970s coincided with higher erosion rates and the warmer-drier periods of the 1970s-1980s with lower erosion rates; gully, mass wasting and fluvial processes exhibit different responses in different basins (Figure 12). We also note that in Coleman basin, where mass wasting measurements were entirely of lateral moraine retreat which we interpret as the result of dry ravel, mass wasting erosion rates are consistent in time and apparently uncorrelated with climate fluctuations. Our observed fluctuations in erosion rates align with results in the literature regarding the sediment yield of glacierized catchments on Mount Rainier. Measurements in Alder Lake, which traps sediment delivered from the south flank of Mount Rainier, indicate large sediment delivery rates between 1945 and 1955, lower sediment delivery rates between 1955 and 1985, and increased sediment delivery thereafter (Czuba et al., 2012).

Because our measurements use a sparse DEM time series, the relationship between climate and erosion rates remains somewhat ambiguous. It is possible that relatively high erosion rates during the earliest measurement period (1947-1970) can be attributed mostly to increased erosion in the

early part of the time interval, following rapid deglaciation between 1930 and 1945 (Dick, 2013). If rapid deglaciation explains the higher erosion rates between 1947 and 1970, it may also explain higher erosion rates after 1980, when glaciers began receding again. However, our measurements of erosion by process indicate that there are areas of erosion far from fluctuating glacier boundaries that follow climate variations (Figure 12) Thus, it appears that while decadal glacier and climate fluctuations are linked, they both can influence erosion rates on different parts of the landscape independently.

6. Conclusion

In a stratovolcano setting in western Washington, we measured erosion processes, their contributions to sediment yields, and how those processes vary in space and time. We determined that no single erosion processes dominates; gully erosion, mass wasting, and glacial erosion related to glacial advance and retreat are responsible for moving similar magnitudes of material, 21.9%, 37.5%, and 40.6% of total sediment yield, respectively.

At the basin-scale, terrain characteristics explain some variability in sediment yield, with drainage area (r^2=0.81), hillslope angle (r^2=0.49), and nonigneous fraction (r^2=0.52) positively correlated and channel slope (r^2=0.62) negatively correlated. Interactions between the predictive variables indicate that volcanic history and the resulting spatial distribution of rock type are important determinants of erosion rates. A fitted model for sediment yield incorporating drainage area and hillslope domain slope of the form $Q = k A^m S_h^n$ performs well (NSE=0.84) and has fitted parameters consistent with the literature. This model reflects the importance of fluid flow on hillslopes, the angle of hillslopes, and, with the low correlation between channel slope and sediment yields, indicates that debris flows, which originate on hillslopes and bypass stream channels, are a primary erosion mechanism in proglacial landscapes.

The spatial distribution of large erosion signals indicates that relict landforms, mostly from LIA glaciation, are the reason for the highly erosive nature of the proglacial landscape. In examining how erosion rates vary in time, we found that climate and short term glacial fluctuations likely influence erosion rates and sediment yields independently. Climate fluctuations exert control on hillslope erosion processes like gullying and landsliding. Glacial fluctuations expose land area to erosive forces and may be directly responsible for erosion through quarrying and plucking processes and indirectly responsible for mass failures by debutressing unstable hillslopes.

At the scale of the larger Nooksack River watershed, we found that proglacial sediments may play an important role and contribute a significant portion of the total load. Our estimates of contributions to stream total load by glacierized headwater basins are highly variable, from 10% to 56%. Annualized sediment yields from glacierized headwater basins exceed contributions to the downstream river systems by channel bank and terrace erosion.

To further develop our understanding of the role of proglacial sediments at the river basin scale, future work should focus on understanding the grain size distributions of proglacial sediments, the travel distance of different grain sizes leaving proglacial basins, and the dynamics of debris flows and other sediment transport processes in intermediate reaches of rivers, which we define as downstream of proglacial basins and upstream of populated lowlands. Future work should also

focus on improving debris flow monitoring in steep, wet mountain ranges and in proglacial regions to better understand the return frequency of hazardous events and the sediment yields associated with these events.

Acknowledgements

We gratefully acknowledge funding support from NSF grant 1663859.

References

Ahnert, F. (1970). Functional relationships between denudation, relief, and uplift in large, mid-latitude drainage basins. *American Journal of Science*, *268*(3).

Ahrendt, S., Horner-Devine, A. R., Collins, B. D., Morgan, J. A., & Istanbulluoglu, E. (2022). Channel Conveyance Variability can Influence Flood Risk as Much as Streamflow Variability in Western Washington State. *Water Resources Research*, *58*(6). https://doi.org/10.1029/2021WR031890

Anderson, S., & Pitlick, J. (2014). Using repeat lidar to estimate sediment transport in a steep stream. *Journal of Geophysical Research: Earth Surface*, *119*(3), 621–643. https://doi.org/10.1002/2013JF002933

Anderson, S. W. (2019). Uncertainty in quantitative analyses of topographic change: Error propagation and the role of thresholding. *Earth Surface Processes and Landforms*, *44*(5), 1015–1033. https://doi.org/10.1002/esp.4551

Anderson, S. W., & Konrad, C. P. (2019). Downstream-Propagating Channel Responses to Decadal-Scale Climate Variability in a Glaciated River Basin. *Journal of Geophysical Research: Earth Surface*, *124*(4), 902–919. https://doi.org/10.1029/2018JF004734

Anderson, S. W., & Shean, D. (2022). Spatial and temporal controls on proglacial erosion rates: A comparison of four basins on Mount Rainier, 1960 to 2017. *Earth Surface Processes and Landforms*, *47*(2), 596–617. https://doi.org/10.1002/esp.5274

Associated press. (2021, November 24). *Washington county's flood damages could reach $50 million*. PBS NewsHour. https://www.pbs.org/newshour/nation/washington-countys-flood-damages-could-reach-50-million

Bartos, M., Itati01, Debbout, R., & Huard, D. (2022). *mdbartos/pysheds: 0.3.3* (0.3.3). Zenodo. https://doi.org/10.5281/ZENODO.6300489

Beason, S. R., Kennard, P. M., Abbe, T. B., & Walkup, L. C. (n.d.). *Landscape response to climate change and its role in infrastructure protection and management at Mount Rainier National Park*. 5.

Beyer, R. A., Alexandrov, O., & McMichael, S. (2018). The Ames Stereo Pipeline: NASA's Open Source Software for Deriving and Processing Terrain Data. *Earth and Space Science*, *5*(9), 537–548. https://doi.org/10.1029/2018EA000409

Beyer, R., Alexandrov, O., & ScottMcMichael. (2019). *NeoGeographyToolkit/StereoPipeline: ASP 2.6.2* (v2.6.2). Zenodo. https://doi.org/10.5281/ZENODO.3247734

Burki, V., Hansen, L., Fredin, O., Andersen, T. A., Beylich, A. A., Jaboyedoff, M., Larsen, E., & Tønnesen, J.-F. (2010). Little Ice Age advance and retreat sediment budgets for an outlet glacier in western Norway. *Boreas*. https://doi.org/10.1111/j.1502-3885.2009.00133.x

Carrivick, J. L., & Heckmann, T. (2017). Short-term geomorphological evolution of proglacial systems. *Geomorphology*, *287*, 3–28. https://doi.org/10.1016/j.geomorph.2017.01.037

Cody, E., Anderson, B. M., McColl, S. T., Fuller, I. C., & Purdie, H. L. (2020). Paraglacial adjustment of sediment slopes during and immediately after glacial debuttressing. *Geomorphology*, *371*, 107411. https://doi.org/10.1016/j.geomorph.2020.107411

Czuba, J. A., & et al. (2012). *Changes in Sediment Volume in Alder Lake, Nisqually River Basin, Washington, 1945–2011* (Open-File Report) [Open-File Report].

Dalton, R. (2021, December 17). *British Columbia floods to cause $2bn economic loss: Aon*. Insurance Insider.

https://www.insuranceinsider.com/article/29gkbiyimu2ar03595jpc/british-columbia-floods-to-cause-2bn-economic-loss-aon
Dick, K. (2000). *Glacier Change in the North Cascades, Washington: 1900-2009*. https://doi.org/10.15760/etd.1062
Dietrich, W. E., Bellugi, D. G., Sklar, L. S., Stock, J. D., Heimsath, A. M., & Roering, J. J. (2013). Geomorphic Transport Laws for Predicting Landscape form and Dynamics. In P. R. Wilcock & R. M. Iverson (Eds.), *Geophysical Monograph Series* (pp. 103–132). American Geophysical Union. https://doi.org/10.1029/135GM09
Fuller, S. R. (n.d.). *Neoglaciation of Avalanche Gorge and the Middle Fork Nooksack River Valley Mt. Baker, Washington*. 78.
Google satellite imagery. (n.d.). Retrieved September 7, 2022, from https://mt1.google.com/vt/lyrs=s&x={x}&y={y}&z={z}
Harper, J. T. (1993). Glacier Terminus Fluctuations on Mount Baker, Washington, U.S.A., 1940-1990, and Climatic Variations. *Arctic and Alpine Research*, *25*(4), 332. https://doi.org/10.2307/1551916
Henck, A. C., Huntington, K. W., Stone, J. O., Montgomery, D. R., & Hallet, B. (2011). Spatial controls on erosion in the Three Rivers Region, southeastern Tibet and southwestern China. *Earth and Planetary Science Letters*, *303*(1–2), 71–83. https://doi.org/10.1016/j.epsl.2010.12.038
Humlum, O. (2000). The geomorphic significance of rock glaciers: Estimates of rock glacier debris volumes and headwall recession rates in West Greenland. *Geomorphology*, *35*(1–2), 41–67. https://doi.org/10.1016/S0169-555X(00)00022-2
Hyde, J., & Crandell, D. (1978). *Postglacial volcanic deposits at Mount Baker, Washington, and potential hazards from future eruptions* (Professional Paper). USGS. https://pubs.er.usgs.gov/publication/pp1022C
Istanbulluoglu, E. (2009). Modeling Catchment Evolution: From Decoding Geomorphic Processes Signatures toward Predicting Impacts of Climate Change: Modeling Catchment Evolution. *Geography Compass*, *3*(3), 1125–1150. https://doi.org/10.1111/j.1749-8198.2009.00228.x
Istanbulluoglu, E., Tarboton, D. G., Pack, R. T., & Luce, C. (2003). A sediment transport model for incision of gullies on steep topography: A TRANSPORT MODEL FOR INCISION OF GULLIES. *Water Resources Research*, *39*(4). https://doi.org/10.1029/2002WR001467
Knuth, F., Schwat, E., Shean, D., & McNeil, C. (2021). *Historical Image Pre-Processing (HIPP) pre-release v0.1* (v0.1). Zenodo. https://doi.org/10.5281/ZENODO.5510876
Knuth, F., Schwat, E., Shean, D., Shashank Bhushan, & Alexandrov, O. (2021). *Historical Structure from Motion (HSfM) pre-release v0.1* (v0.1). Zenodo. https://doi.org/10.5281/ZENODO.5510870
Knuth, F., Shean, D., Schwat, E., Alexandrov, O., McNeil, C., Dehecq, A., Florentine, C., & O'Neel. (in review). Historical Structure from Motion (HSfM): Automated processing of historical aerial photographs for long-term geodetic change analysis. *Remote Sensing of the Environment*.
Lancaster, S. T., Nolin, A. W., Copeland, E. A., & Grant, G. E. (2012). Periglacial debris-flow initiation and susceptibility and glacier recession from imagery, airborne LiDAR, and ground-based mapping. *Geosphere*, *8*(2), 417–430. https://doi.org/10.1130/GES00713.1
Lane, S. N., Bakker, M., Gabbud, C., Micheletti, N., & Saugy, J.-N. (2017). Sediment export, transient landscape response and catchment-scale connectivity following rapid climate

warming and Alpine glacier recession. *Geomorphology*, *277*, 210–227. https://doi.org/10.1016/j.geomorph.2016.02.015

Lee, S. Y., & Hamlet, A. F. (2011). *Skagit River Basin Climate Science Report, a summary report prepared for Skagit County and the Envision Skagit Project by the Department of Civil and Environmental Engineering and The Climate Impacts Group at the University of Washington.* http://ftp.hydro.washington.edu/pub/hamleaf/skagit_report/final/

Legg, N. T., Meigs, A. J., Grant, G. E., & Kennard, P. (2014). Debris flow initiation in proglacial gullies on Mount Rainier, Washington. *Geomorphology*, *226*, 249–260. https://doi.org/10.1016/j.geomorph.2014.08.003

Mancini, D., & Lane, S. N. (2020). Changes in sediment connectivity following glacial debuttressing in an Alpine valley system. *Geomorphology*, *352*, 106987. https://doi.org/10.1016/j.geomorph.2019.106987

Mariotti, A., Blard, P.-H., Charreau, J., Toucanne, S., Jorry, S. J., Molliex, S., Bourlès, D. L., Aumaître, G., & Keddadouche, K. (2021). Nonlinear forcing of climate on mountain denudation during glaciations. *Nature Geoscience*, *14*(1), 16–22. https://doi.org/10.1038/s41561-020-00672-2

Montgomery, D. R., & Brandon, M. T. (2002). Topographic controls on erosion rates in tectonically active mountain ranges. *Earth and Planetary Science Letters*, *201*(3–4), 481–489. https://doi.org/10.1016/S0012-821X(02)00725-2

Moore, R. D., Fleming, S. W., Menounos, B., Wheate, R., Fountain, A., Stahl, K., Holm, K., & Jakob, M. (2009). Glacier change in western North America: Influences on hydrology, geomorphic hazards and water quality. *Hydrological Processes*, *23*(1), 42–61. https://doi.org/10.1002/hyp.7162

Nolan, D. M., Post, A. S., Hauer, W., Zinck, A., & O'Neel, S. (2017). *Photogrammetric scans of aerial photographs of North American glaciers* [Text/xml]. NSF Arctic Data Center. https://doi.org/10.18739/A2VH5CJ8K

Nuth, C., & Kääb, A. (2011). Co-registration and bias corrections of satellite elevation data sets for quantifying glacier thickness change. *The Cryosphere*, *5*(1), 271–290. https://doi.org/10.5194/tc-5-271-2011

Portenga, E. W., & Bierman, P. R. (2011). Understanding Earth's eroding surface with 10Be. *GSA Today*, *21*(8), 4–10. https://doi.org/10.1130/G111A.1

Prancevic, J. P., Lamb, M. P., & Fuller, B. M. (2014). Incipient sediment motion across the river to debris-flow transition. *Geology*, *42*(3), 191–194. https://doi.org/10.1130/G34927.1

Ramsey, D. (2017). *Mt. Baker LiDAR Technical Report*. USGS.

RGI Consortium. (2017). *Randolph Glacier Inventory—A Dataset of Global Glacier Outlines, Version 6* [Data set]. National Snow and Ice Data Center. https://doi.org/10.7265/4M1F-GD79

Roe, G. H., & O'Neal, M. A. (2009). The response of glaciers to intrinsic climate variability: Observations and models of late-Holocene variations in the Pacific Northwest. *Journal of Glaciology*, *55*(193), 839–854. https://doi.org/10.3189/002214309790152438

Rolstad, C., Haug, T., & Denby, B. (2009). Spatially integrated geodetic glacier mass balance and its uncertainty based on geostatistical analysis: Application to the western Svartisen ice cap, Norway. *Journal of Glaciology*, *55*(192), 666–680. https://doi.org/10.3189/002214309789470950

Scott Anderson & et al. (2019). *Sediment Storage and Transport in the Nooksack River Basin, Northwestern Washington, 2006–15* (Scientific Investigations Report) [Scientific Investigations Report].

Scott, D. N., & Collins, B. D. (2021). Frequent Mass Movements From Glacial and Lahar Terraces, Controlled by Both Hillslope Characteristics and Fluvial Erosion, are an Important Sediment Source to Puget Sound Rivers. *Water Resources Research*, *57*(4). https://doi.org/10.1029/2020WR028389

Scott, K., Hildreth, W., & Gardner, C. (2000). *Mount Baker—Living with an active volcano* (Fact Sheet) [Fact Sheet]. United States Geological Survey.

Shean, D., Shashank Bhushan, Lilien, D., Knuth, F., Schwat, E., Meyer, J., Sharp, M., & Hu, M. (2021). *dshean/demcoreg: V1.1.0* (v1.1.0). Zenodo. https://doi.org/10.5281/ZENODO.5733347

Stock, J. D., & Montgomery, D. R. (1999). Geologic constraints on bedrock river incision using the stream power law. *Journal of Geophysical Research: Solid Earth*, *104*(B3), 4983–4993. https://doi.org/10.1029/98JB02139

Strauch, R., Istanbulluoglu, E., & Riedel, J. (2019). A new approach to mapping landslide hazards: A probabilistic integration of empirical and physically based models in the North Cascades of Washington, USA. *Natural Hazards and Earth System Sciences*, *19*(11), 2477–2495. https://doi.org/10.5194/nhess-19-2477-2019

Tabor, R. W., Haugerud, R. A., Hildreth, W., & Brown, E. H. (2003). *Geologic Map of the Mount Baker 30- by 60-Minute Quadrangle, Washington*. https://pubs.usgs.gov/imap/i2660/

Tucker, D. S., Scott, K. M., Grossman, E. E., & Linneman, S. (2014). Mount Baker lahars and debris flows, ancient, modern, and future. *GSA Field Guides*, *38*, 33–52. USGS Publications Warehouse. https://doi.org/10.1130/2014.0038(03)

Turowski, J. M., Rickenmann, D., & Dadson, S. J. (2010). The partitioning of the total sediment load of a river into suspended load and bedload: A review of empirical data: The partitioning of sediment load. *Sedimentology*, *57*(4), 1126–1146. https://doi.org/10.1111/j.1365-3091.2009.01140.x

U.S.G.S. (2016). *The StreamStats program*. United States Geological Survey. http://streamstats.usgs.gov

Virtanen, P., Gommers, R., Oliphant, T. E., Haberland, M., Reddy, T., Cournapeau, D., Burovski, E., Peterson, P., Weckesser, W., Bright, J., van der Walt, S. J., Brett, M., Wilson, J., Millman, K. J., Mayorov, N., Nelson, A. R. J., Jones, E., Kern, R., Larson, E., … Vázquez-Baeza, Y. (2020). SciPy 1.0: Fundamental algorithms for scientific computing in Python. *Nature Methods*, *17*(3), 261–272. https://doi.org/10.1038/s41592-019-0686-2

Wood, C. A. (Ed.). (1992). *Volcanoes of North America: United States and Canada* (1. paperback ed). Cambridge Univ. Pr.

Xdem Contributors. (2021). *Xdem* (v0.0.2). Zenodo. https://doi.org/10.5281/ZENODO.4809698

Supplementary Information

Figure S1. Red polygons show the manually identified static bareground identified on Mount Baker for analysis of the uncertainty of DEMs of Difference (DoDs).

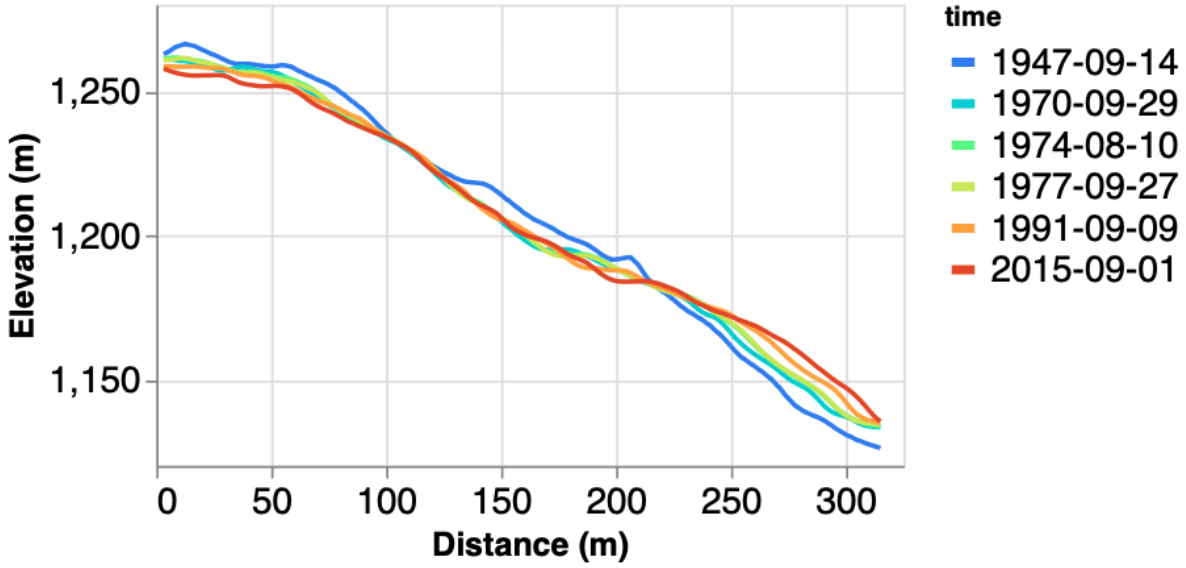

Figure S2. Transect evolution of the rotational slip/sackung in Rainbow basin. See Transect 3 in Figure 4.

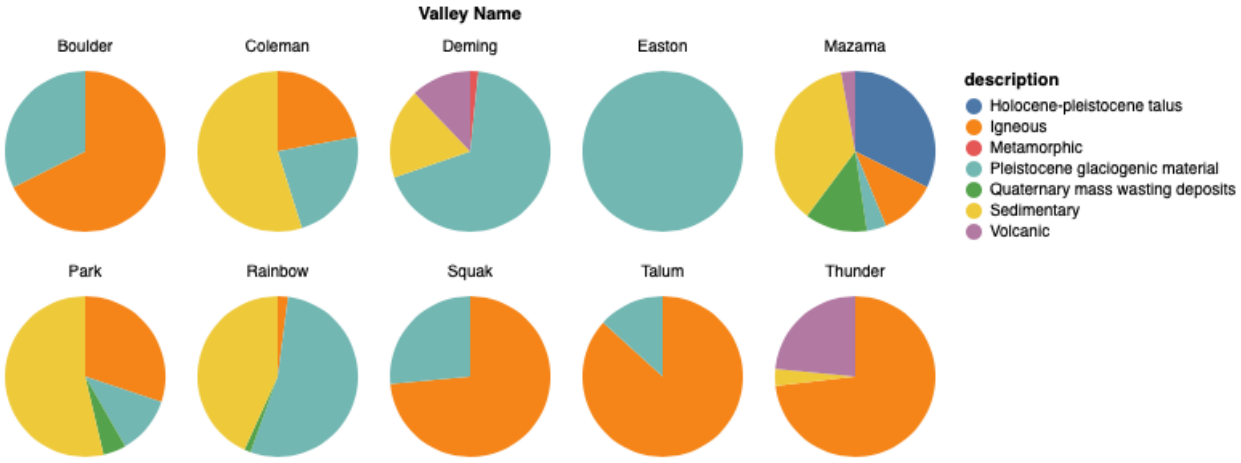

Figure S3. Proportion of surface area in each valley covered by different geological units. Proportions were calculated by cropping a bedrock geologic map (Tabor et al., 2003) by the combined hillslope and fluvial domain polygons.

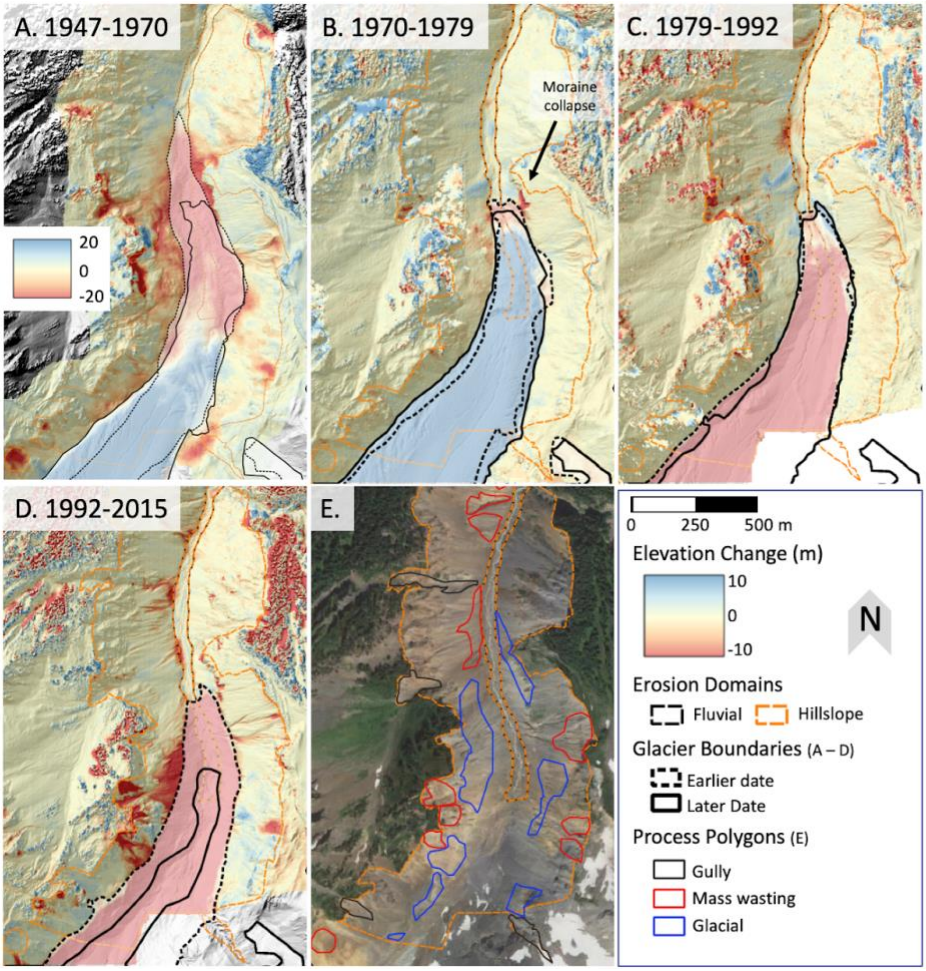

Figure S4. (A - D) Mazama glacial valley DoDs shown for 4 time intervals, DoDs are overlaid on DEM hillshades from the later date. Elevation changes beyond the range -10 to 10 meters have the same color as changes of -10 and 10 meters. Opaque polygons cover elevation changes related to changing glacial extent. Panel (A) has a different color scale, shown inset in the panel. (E) Erosion domains and process polygons overlain on Google satellite imagery (citation).

Table S1. Glacier footprint areas during four time periods. Years and time periods use 1977 for Rainbow and Park glaciers, 1979 for all other glaciers. Observed glacial maxima is the year in which the glacier reached furthest downhill. Note the unique behavior of Mazama glacier, which 1947 retreated upslope after 1947 (terminus elevation increased) but grew in footprint size as well. Glacial area change estimates are conservative, as RGI polygons were only modified for our study in the immediate area of the measured proglacial basins.

Glacier	Year with observed glacier termini maxima	Glacier Area (km^2)	Glacier Area Change (km^2)		Glacier Area Change (%)		Glacier Area (km^2), reported by Dick (2013	Glacier Area Change (%), reported by Dick (2013)	
		1947	1947 - 1977/9	1977/9 - 2015	1947 - 1977/9	1977/9 - 2015	1947	1947 - 1977/9	1977/9 - 2009
Boulder	1979	5.5	0.93	-0.80	17	-12	3.4	19	-15
Coleman	1979	6.5	0.66	-0.42	10	-5.8	4.64	10	-10
Deming	1979	4.9	0.20	-0.37	4.0	-7.2	4.75	10	-9.2
Easton	1991	2.6	0.25	-0.19	9.6	-6.4	2.65	8.7	-6.9
Mazama	1947	5.5	0.068	-0.56	1.2	-10	5.4 (1975)	-	-
Park	1979	2.7	0.55	-0.39	20	-12	3.1 (1975)	-	-
Rainbow	1979	2.3	0.37	-0.69	16	-25	1.7	7.6	-8.2
Roosevelt	1979	3.4	0.38	-0.24	11	-6.4	3.74	11	-12
Squak	1979	1.9	0.39	-0.36	20	-15	2.1 (1975)	-	-
Talum	1979	1.9	0.50	-0.48	26	-20	2.2 (1975)	-	-
Thunder	1979	0.94	0.027	-0.18	2.9	-19			

Table S2. Gross positive and negative annualized rate of volumetric change in 1,000s of m^3/yr.

valley	process	type	start_time	end_time	Annual Mass Wasted	Uncertainty
Coleman	**fluvial**	**negative**	**1947-09-14**	**1970-09-29**	**-2.39**	**1.04**
Coleman	**fluvial**	**negative**	**1970-09-29**	**1979-10-06**	**-0.06**	**0.51**
Coleman	**fluvial**	**negative**	**1979-10-06**	**1987-08-21**	**-0.27**	**0.89**
Coleman	**fluvial**	**negative**	**1987-08-21**	**1990-09-05**	**-0.58**	**8.46**
Coleman	**fluvial**	**negative**	**1990-09-05**	**2015-09-01**	**-2.13**	**0.35**

Coleman	**fluvial**	**positive**	**1947-09-14**	**1970-09-29**	**0.08**	**1.03**
Coleman	**fluvial**	**positive**	**1970-09-29**	**1979-10-06**	**1.09**	**0.50**
Coleman	**fluvial**	**positive**	**1979-10-06**	**1987-08-21**	**1.20**	**0.90**
Coleman	**fluvial**	**positive**	**1987-08-21**	**1990-09-05**	**0.02**	**8.46**
Coleman	**fluvial**	**positive**	**1990-09-05**	**2015-09-01**	**0.03**	**0.35**
Coleman	**hillslope**	**negative**	**1947-09-14**	**1970-09-29**	**-45.34**	**12.13**
Coleman	**hillslope**	**negative**	**1970-09-29**	**1979-10-06**	**-8.41**	**15.92**
Coleman	**hillslope**	**negative**	**1979-10-06**	**1987-08-21**	**-9.04**	**26.81**
Coleman	**hillslope**	**negative**	**1987-08-21**	**1990-09-05**	**-28.14**	**127.61**
Coleman	**hillslope**	**negative**	**1990-09-05**	**2015-09-01**	**-13.36**	**2.92**
Coleman	**hillslope**	**positive**	**1947-09-14**	**1970-09-29**	**4.43**	**12.13**
Coleman	**hillslope**	**positive**	**1970-09-29**	**1979-10-06**	**16.25**	**15.92**
Coleman	**hillslope**	**positive**	**1979-10-06**	**1987-08-21**	**10.96**	**26.81**
Coleman	**hillslope**	**positive**	**1987-08-21**	**1990-09-05**	**2.19**	**127.61**
Coleman	**hillslope**	**positive**	**1990-09-05**	**2015-09-01**	**3.84**	**2.93**
Deming	**fluvial**	**negative**	**1947-09-14**	**1970-09-29**	**-16.83**	**1.34**
Deming	**fluvial**	**negative**	**1970-09-29**	**1979-10-06**	**-0.58**	**3.55**
Deming	**fluvial**	**negative**	**1979-10-06**	**1991-09-09**	**-0.83**	**0.29**
Deming	**fluvial**	**negative**	**1991-09-09**	**2015-09-01**	**-10.21**	**0.53**
Deming	**fluvial**	**positive**	**1947-09-14**	**1970-09-29**	**1.42**	**1.35**
Deming	**fluvial**	**positive**	**1970-09-29**	**1979-10-06**	**18.59**	**3.55**
Deming	**fluvial**	**positive**	**1979-10-06**	**1991-09-09**	**6.77**	**0.29**
Deming	**fluvial**	**positive**	**1991-09-09**	**2015-09-01**	**1.15**	**0.52**
Deming	**hillslope**	**negative**	**1947-09-14**	**1970-09-29**	**-112.93**	**6.38**
Deming	**hillslope**	**negative**	**1970-09-29**	**1979-10-06**	**-20.54**	**17.09**
Deming	**hillslope**	**negative**	**1979-10-06**	**1991-09-09**	**-25.27**	**0.99**
Deming	**hillslope**	**negative**	**1991-09-09**	**2015-09-01**	**-57.48**	**2.73**
Deming	**hillslope**	**positive**	**1947-09-14**	**1970-09-29**	**5.81**	**6.38**

Deming	**hillslope**	**positive**	**1970-09-29**	**1979-10-06**	**52.51**	**17.09**
Deming	**hillslope**	**positive**	**1979-10-06**	**1991-09-09**	**24.40**	**0.98**
Deming	**hillslope**	**positive**	**1991-09-09**	**2015-09-01**	**5.03**	**2.73**
Mazama	**fluvial**	**negative**	**1947-09-14**	**1970-09-29**	**-0.91**	**1.06**
Mazama	**fluvial**	**negative**	**1970-09-29**	**1979-10-06**	**-0.78**	**0.45**
Mazama	**fluvial**	**negative**	**1979-10-06**	**1992-09-18**	**-3.00**	**1.28**
Mazama	**fluvial**	**negative**	**1992-09-18**	**2015-09-01**	**-2.59**	**0.89**
Mazama	**fluvial**	**positive**	**1947-09-14**	**1970-09-29**	**0.51**	**1.05**
Mazama	**fluvial**	**positive**	**1970-09-29**	**1979-10-06**	**2.13**	**0.46**
Mazama	**fluvial**	**positive**	**1979-10-06**	**1992-09-18**	**0.96**	**1.28**
Mazama	**fluvial**	**positive**	**1992-09-18**	**2015-09-01**	**0.37**	**0.88**
Mazama	**hillslope**	**negative**	**1947-09-14**	**1970-09-29**	**-103.12**	**36.56**
Mazama	**hillslope**	**negative**	**1970-09-29**	**1979-10-06**	**-30.01**	**7.73**
Mazama	**hillslope**	**negative**	**1979-10-06**	**1992-09-18**	**-23.64**	**18.56**
Mazama	**hillslope**	**negative**	**1992-09-18**	**2015-09-01**	**-40.68**	**6.03**
Mazama	**hillslope**	**positive**	**1947-09-14**	**1970-09-29**	**15.66**	**36.56**
Mazama	**hillslope**	**positive**	**1970-09-29**	**1979-10-06**	**37.70**	**7.73**
Mazama	**hillslope**	**positive**	**1979-10-06**	**1992-09-18**	**15.41**	**18.56**
Mazama	**hillslope**	**positive**	**1992-09-18**	**2015-09-01**	**8.57**	**6.04**
Rainbow	**fluvial**	**negative**	**1947-09-14**	**1970-09-29**	**-6.00**	**1.22**
Rainbow	**fluvial**	**negative**	**1970-09-29**	**1974-08-10**	**0.00**	**1.97**
Rainbow	**fluvial**	**negative**	**1974-08-10**	**1977-09-27**	**-0.37**	**0.94**
Rainbow	**fluvial**	**negative**	**1977-09-27**	**1991-09-09**	**-0.42**	**0.17**
Rainbow	**fluvial**	**negative**	**1991-09-09**	**2015-09-01**	**-1.55**	**0.14**
Rainbow	**fluvial**	**positive**	**1947-09-14**	**1970-09-29**	**9.10**	**1.22**
Rainbow	**fluvial**	**positive**	**1970-09-29**	**1974-08-10**	**0.96**	**1.98**
Rainbow	**fluvial**	**positive**	**1974-08-10**	**1977-09-27**	**0.80**	**0.94**
Rainbow	**fluvial**	**positive**	**1977-09-27**	**1991-09-09**	**0.45**	**0.16**

Rainbow	**fluvial**	**positive**	**1991-09-09**	**2015-09-01**	**1.36**	**0.14**
Rainbow	**hillslope**	**negative**	**1947-09-14**	**1970-09-29**	**-105.99**	**15.43**
Rainbow	**hillslope**	**negative**	**1970-09-29**	**1974-08-10**	**-40.32**	**40.62**
Rainbow	**hillslope**	**negative**	**1974-08-10**	**1977-09-27**	**-43.36**	**17.11**
Rainbow	**hillslope**	**negative**	**1977-09-27**	**1991-09-09**	**-18.03**	**2.41**
Rainbow	**hillslope**	**negative**	**1991-09-09**	**2015-09-01**	**-22.61**	**1.66**
Rainbow	**hillslope**	**positive**	**1947-09-14**	**1970-09-29**	**21.88**	**15.43**
Rainbow	**hillslope**	**positive**	**1970-09-29**	**1974-08-10**	**51.53**	**40.61**
Rainbow	**hillslope**	**positive**	**1974-08-10**	**1977-09-27**	**50.36**	**17.11**
Rainbow	**hillslope**	**positive**	**1977-09-27**	**1991-09-09**	**12.80**	**2.40**
Rainbow	**hillslope**	**positive**	**1991-09-09**	**2015-09-01**	**8.08**	**1.66**

Table S3. Cumulative net volumetric change, in 1,000s of m^3/yr. When "bounding" is TRUE, the DoD used for measurement is the 1947-2015 DoD, which represents measurements over our entire study time period. Uncertainty values presented for cumulative totals over the entire measurement periods are the sum-of-squares of uncertainties associated with each accumulated measurement.

valley	type	end_time	cumulative volume	bounding	uncertainty
Coleman	**all**	**1947-09-14**	**0.00**	**FALSE**	
Coleman	**all**	**1970-09-29**	**-1187.94**	**FALSE**	
Coleman	**all**	**1979-10-06**	**-1129.82**	**FALSE**	
Coleman	**all**	**1987-08-21**	**-1129.73**	**FALSE**	
Coleman	**all**	**1990-09-05**	**-1084.42**	**FALSE**	
Coleman	**all**	**2015-09-01**	**-1404.11**	**FALSE**	**578.84**
Coleman	**fluvial**	**1947-09-14**	**0.00**	**FALSE**	
Coleman	**fluvial**	**1970-09-29**	**-75.93**	**FALSE**	
Coleman	**fluvial**	**1979-10-06**	**-66.86**	**FALSE**	

Coleman	**fluvial**	**1987-08-21**	**-59.18**	**FALSE**	
Coleman	**fluvial**	**1990-09-05**	**-51.64**	**FALSE**	
Coleman	**fluvial**	**2015-09-01**	**-113.01**	**FALSE**	**36.89**
Coleman	**fluvial**	**2018-05-28**	**-96.87**	**TRUE**	**19.98**
Coleman	**glacial**	**1947-09-14**	**0.00**	**FALSE**	
Coleman	**glacial**	**1970-09-29**	**-227.63**	**FALSE**	
Coleman	**glacial**	**1979-10-06**	**-227.42**	**FALSE**	
Coleman	**glacial**	**1987-08-21**	**-227.19**	**FALSE**	
Coleman	**glacial**	**1990-09-05**	**-212.76**	**FALSE**	
Coleman	**glacial**	**2015-09-01**	**-256.06**	**FALSE**	**25.05**
Coleman	**glacial**	**2018-05-28**	**-770.41**	**TRUE**	**19.44**
Coleman	**gully**	**1947-09-14**	**0.00**	**FALSE**	
Coleman	**gully**	**1970-09-29**	**-22.52**	**FALSE**	
Coleman	**gully**	**1979-10-06**	**-22.31**	**FALSE**	
Coleman	**gully**	**1987-08-21**	**-20.30**	**FALSE**	
Coleman	**gully**	**1990-09-05**	**-21.54**	**FALSE**	
Coleman	**gully**	**2015-09-01**	**-24.35**	**FALSE**	**5.05**
Coleman	**gully**	**2018-05-28**	**-24.34**	**TRUE**	**1.64**
Coleman	**hillslope**	**1947-09-14**	**0.00**	**FALSE**	
Coleman	**hillslope**	**1970-09-29**	**-1109.39**	**FALSE**	

Coleman	**hillslope**	**1979-10-06**	**-1059.67**	**FALSE**	
Coleman	**hillslope**	**1987-08-21**	**-1067.76**	**FALSE**	
Coleman	**hillslope**	**1990-09-05**	**-1030.11**	**FALSE**	
Coleman	**hillslope**	**2015-09-01**	**-1289.36**	**FALSE**	**544.33**
Coleman	**hillslope**	**2018-05-28**	**-2486.68**	**TRUE**	**251.12**
Coleman	**mass wasting**	**1947-09-14**	**0.00**	**FALSE**	
Coleman	**mass wasting**	**1970-09-29**	**-295.87**	**FALSE**	
Coleman	**mass wasting**	**1979-10-06**	**-356.20**	**FALSE**	
Coleman	**mass wasting**	**1987-08-21**	**-385.40**	**FALSE**	
Coleman	**mass wasting**	**1990-09-05**	**-413.95**	**FALSE**	
Coleman	**mass wasting**	**2015-09-01**	**-555.50**	**FALSE**	**114.57**
Coleman	**mass wasting**	**2018-05-28**	**-555.32**	**TRUE**	**25.43**
Deming	**all**	**1947-09-14**	**0.00**	**FALSE**	
Deming	**all**	**1970-09-29**	**-2933.34**	**FALSE**	
Deming	**all**	**1979-10-06**	**-2344.21**	**FALSE**	
Deming	**all**	**1991-09-09**	**-2214.66**	**FALSE**	
Deming	**all**	**2015-09-01**	**-3647.33**	**FALSE**	**268.71**
Deming	**fluvial**	**1947-09-14**	**0.00**	**FALSE**	
Deming	**fluvial**	**1970-09-29**	**-394.25**	**FALSE**	
Deming	**fluvial**	**1979-10-06**	**-219.87**	**FALSE**	

Deming	**fluvial**	**1991-09-09**	**-137.10**	**FALSE**	
Deming	**fluvial**	**2015-09-01**	**-354.67**	**FALSE**	**46.34**
Deming	**fluvial**	**2018-05-28**	**-406.06**	**TRUE**	**49.66**
Deming	**glacial**	**1947-09-14**	**0.00**	**FALSE**	
Deming	**glacial**	**1970-09-29**	**-648.91**	**FALSE**	
Deming	**glacial**	**1979-10-06**	**-612.93**	**FALSE**	
Deming	**glacial**	**1991-09-09**	**-608.73**	**FALSE**	
Deming	**glacial**	**2015-09-01**	**-1265.88**	**FALSE**	**25.64**
Deming	**glacial**	**2018-05-28**	**-1468.26**	**TRUE**	**62.58**
Deming	**gully**	**1947-09-14**	**0.00**	**FALSE**	
Deming	**gully**	**1970-09-29**	**-238.19**	**FALSE**	
Deming	**gully**	**1979-10-06**	**-260.84**	**FALSE**	
Deming	**gully**	**1991-09-09**	**-297.79**	**FALSE**	
Deming	**gully**	**2015-09-01**	**-347.52**	**FALSE**	**12.83**
Deming	**gully**	**2018-05-28**	**-347.13**	**TRUE**	**12.28**
Deming	**hillslope**	**1947-09-14**	**0.00**	**FALSE**	
Deming	**hillslope**	**1970-09-29**	**-2536.62**	**FALSE**	
Deming	**hillslope**	**1979-10-06**	**-2124.47**	**FALSE**	
Deming	**hillslope**	**1991-09-09**	**-2072.50**	**FALSE**	
Deming	**hillslope**	**2015-09-01**	**-3284.46**	**FALSE**	**222.81**

Deming	**hillslope**	**2018-05-28**	**-2920.80**	**TRUE**	**257.84**
Deming	**mass wasting**	**1947-09-14**	**0.00**	**FALSE**	
Deming	**mass wasting**	**1970-09-29**	**-950.68**	**FALSE**	
Deming	**mass wasting**	**1979-10-06**	**-864.21**	**FALSE**	
Deming	**mass wasting**	**1991-09-09**	**-879.32**	**FALSE**	
Deming	**mass wasting**	**2015-09-01**	**-979.72**	**FALSE**	**53.65**
Deming	**mass wasting**	**2018-05-28**	**-982.30**	**TRUE**	**51.38**
Mazama	**all**	**1947-09-14**	**0.00**	**FALSE**	
Mazama	**all**	**1970-09-29**	**-1714.71**	**FALSE**	
Mazama	**all**	**1979-10-06**	**-1495.81**	**FALSE**	
Mazama	**all**	**1992-09-18**	**-1739.53**	**FALSE**	
Mazama	**all**	**2015-09-01**	**-2529.23**	**FALSE**	**914.96**
Mazama	**fluvial**	**1947-09-14**	**0.00**	**FALSE**	
Mazama	**fluvial**	**1970-09-29**	**-5.84**	**FALSE**	
Mazama	**fluvial**	**1979-10-06**	**16.07**	**FALSE**	
Mazama	**fluvial**	**1992-09-18**	**-23.19**	**FALSE**	
Mazama	**fluvial**	**2015-09-01**	**-78.71**	**FALSE**	**36.04**
Mazama	**fluvial**	**2018-05-28**	**-60.55**	**TRUE**	**20.63**
Mazama	**glacial**	**1947-09-14**	**0.00**	**FALSE**	
Mazama	**glacial**	**1970-09-29**	**-367.31**	**FALSE**	

Mazama	**glacial**	**1979-10-06**	**-384.80**	**FALSE**	
Mazama	**glacial**	**1992-09-18**	**-382.28**	**FALSE**	
Mazama	**glacial**	**2015-09-01**	**-474.37**	**FALSE**	**55.00**
Mazama	**glacial**	**2018-05-28**	**-683.93**	**TRUE**	**50.05**
Mazama	**gully**	**1947-09-14**	**0.00**	**FALSE**	
Mazama	**gully**	**1970-09-29**	**-111.65**	**FALSE**	
Mazama	**gully**	**1979-10-06**	**-102.94**	**FALSE**	
Mazama	**gully**	**1992-09-18**	**-164.60**	**FALSE**	
Mazama	**gully**	**2015-09-01**	**-213.04**	**FALSE**	**39.73**
Mazama	**gully**	**2018-05-28**	**-212.98**	**TRUE**	**27.37**
Mazama	**hillslope**	**1947-09-14**	**0.00**	**FALSE**	
Mazama	**hillslope**	**1970-09-29**	**-1742.64**	**FALSE**	
Mazama	**hillslope**	**1979-10-06**	**-1537.86**	**FALSE**	
Mazama	**hillslope**	**1992-09-18**	**-1743.52**	**FALSE**	
Mazama	**hillslope**	**2015-09-01**	**-2489.06**	**FALSE**	**888.44**
Mazama	**hillslope**	**2018-05-28**	**-2802.33**	**TRUE**	**667.82**
Mazama	**mass wasting**	**1947-09-14**	**0.00**	**FALSE**	
Mazama	**mass wasting**	**1970-09-29**	**-244.44**	**FALSE**	
Mazama	**mass wasting**	**1979-10-06**	**-248.80**	**FALSE**	
Mazama	**mass wasting**	**1992-09-18**	**-332.96**	**FALSE**	

Mazama	**mass wasting**	**2015-09-01**	**-609.80**	**FALSE**	**95.40**
Mazama	**mass wasting**	**2018-05-28**	**-604.45**	**TRUE**	**67.17**
Rainbow	**all**	**1947-09-14**	**0.00**	**FALSE**	
Rainbow	**all**	**1970-09-29**	**-2095.93**	**FALSE**	
Rainbow	**all**	**1974-08-10**	**-2085.11**	**FALSE**	
Rainbow	**all**	**1977-09-27**	**-2041.28**	**FALSE**	
Rainbow	**all**	**1991-09-09**	**-2072.41**	**FALSE**	
Rainbow	**all**	**2015-09-01**	**-2433.23**	**FALSE**	**426.20**
Rainbow	**fluvial**	**1947-09-14**	**0.00**	**FALSE**	
Rainbow	**fluvial**	**1970-09-29**	**90.46**	**FALSE**	
Rainbow	**fluvial**	**1974-08-10**	**101.37**	**FALSE**	
Rainbow	**fluvial**	**1977-09-27**	**108.93**	**FALSE**	
Rainbow	**fluvial**	**1991-09-09**	**107.05**	**FALSE**	
Rainbow	**fluvial**	**2015-09-01**	**101.55**	**FALSE**	**29.63**
Rainbow	**fluvial**	**2018-05-28**	**128.26**	**TRUE**	**38.68**
Rainbow	**glacial**	**1947-09-14**	**0.00**	**FALSE**	
Rainbow	**glacial**	**1970-09-29**	**-24.86**	**FALSE**	
Rainbow	**glacial**	**1974-08-10**	**-24.86**	**FALSE**	
Rainbow	**glacial**	**1977-09-27**	**-24.86**	**FALSE**	
Rainbow	**glacial**	**1991-09-09**	**-24.86**	**FALSE**	

Rainbow	**glacial**	**2015-09-01**	**-24.86**	**FALSE**	**1.17**
Rainbow	**glacial**	**2018-05-28**	**-324.89**	**TRUE**	**16.38**
Rainbow	**gully**	**1947-09-14**	**0.00**	**FALSE**	
Rainbow	**gully**	**1970-09-29**	**-665.04**	**FALSE**	
Rainbow	**gully**	**1974-08-10**	**-703.52**	**FALSE**	
Rainbow	**gully**	**1977-09-27**	**-742.45**	**FALSE**	
Rainbow	**gully**	**1991-09-09**	**-817.80**	**FALSE**	
Rainbow	**gully**	**2015-09-01**	**-1115.52**	**FALSE**	**63.74**
Rainbow	**gully**	**2018-05-28**	**-1162.24**	**TRUE**	**78.83**
Rainbow	**hillslope**	**1947-09-14**	**0.00**	**FALSE**	
Rainbow	**hillslope**	**1970-09-29**	**-2186.44**	**FALSE**	
Rainbow	**hillslope**	**1974-08-10**	**-2186.48**	**FALSE**	
Rainbow	**hillslope**	**1977-09-27**	**-2150.13**	**FALSE**	
Rainbow	**hillslope**	**1991-09-09**	**-2179.35**	**FALSE**	
Rainbow	**hillslope**	**2015-09-01**	**-2535.30**	**FALSE**	**397.16**
Rainbow	**hillslope**	**2018-05-28**	**-2885.38**	**TRUE**	**541.73**
Rainbow	**mass wasting**	**1947-09-14**	**0.00**	**FALSE**	
Rainbow	**mass wasting**	**1970-09-29**	**-819.82**	**FALSE**	
Rainbow	**mass wasting**	**1974-08-10**	**-841.28**	**FALSE**	
Rainbow	**mass wasting**	**1977-09-27**	**-830.85**	**FALSE**	

Rainbow	**mass wasting**	**1991-09-09**	**-832.85**	**FALSE**	
Rainbow	**mass wasting**	**2015-09-01**	**-854.87**	**FALSE**	**27.73**
Rainbow	**mass wasting**	**2018-05-28**	**-858.58**	**TRUE**	**33.36**

Table S4. Annualized net mass wasted (net volumetric change) and calculated sediment yields for the entire measurement period (1947-2015).

Valley Name	Fork of the Nooksack River	Annual Mass Wasted	uncertainty (annual mass wasted)	sediment yield (kt / yr)	uncertainty (Sediment yield)
Park	**Does not drain to Nooksack River**	**29.80**	**4.38**	**50.36**	**7.40**
Rainbow	**Does not drain to Nooksack River**	**42.30**	**6.25**	**71.49**	**10.6**
Boulder	**Does not drain to Nooksack River**	**6.42**	**10.41**	**10.85**	**17.6**
Squak	**Does not drain to Nooksack River**	**-7.23**	**5.40**	**-12.21**	**9.13**
Thunder	**Middle Fork**	**2.74**	**8.02**	**4.64**	**14.6**
Talum	**Does not drain to Nooksack River**	**-12.37**	**6.49**	**-20.90**	**11.0**
Easton	**Does not drain to Nooksack River**	**13.16**	**3.59**	**22.24**	**6.07**
Deming	**Middle Fork**	**57.55**	**5.22**	**97.26**	**8.82**
Coleman	**North Fork**	**51.08**	**4.36**	**86.32**	**7.37**
Mazama	**North Fork**	**46.88**	**11.88**	**79.23**	**20.1**

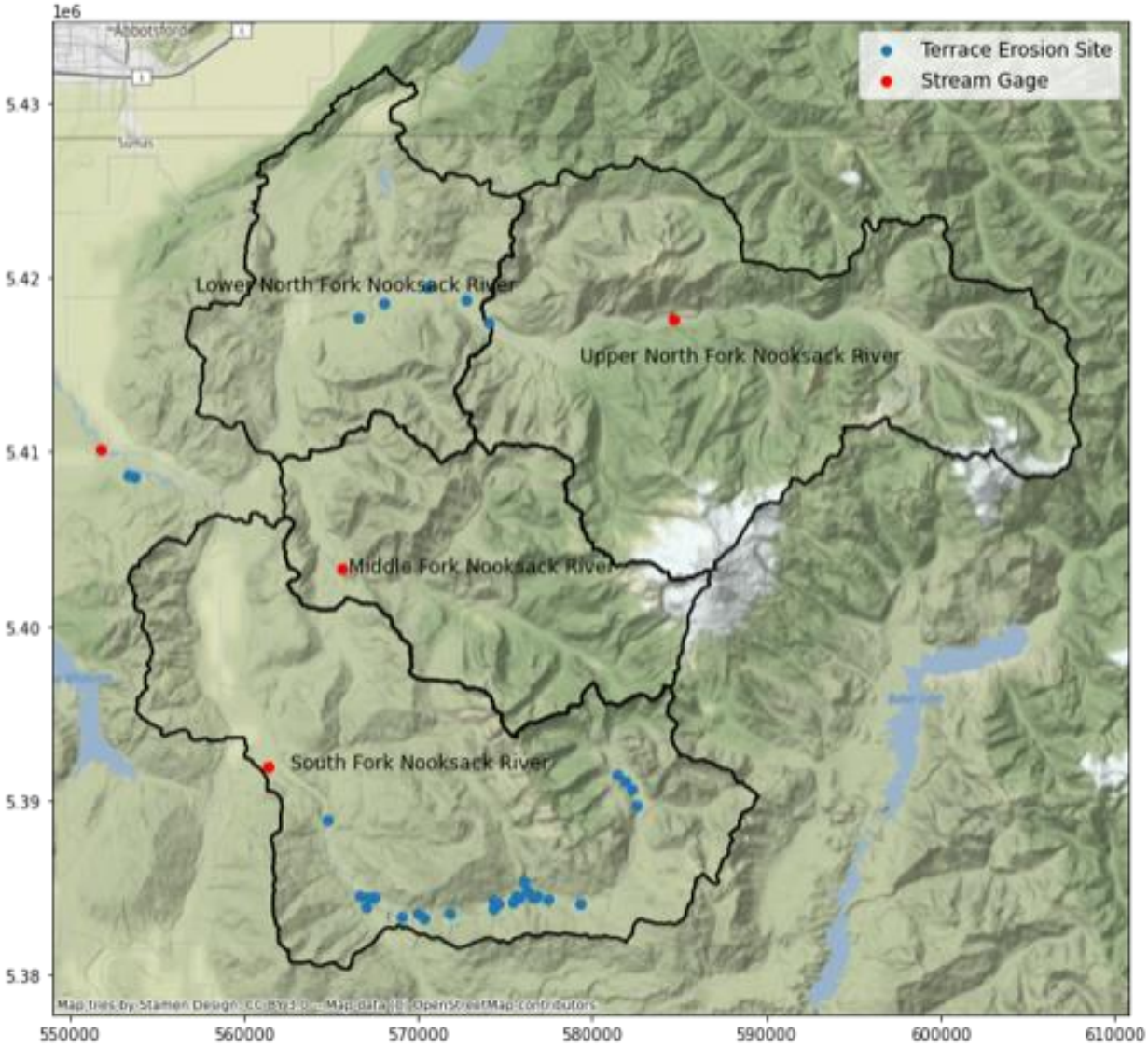

Figure S6. Reanalysis of Scott and Collins (2021) terrace erosion study. Blue dots show the locations of mapped terrace erosion sites in the Nooksack river basin, locations taken from the supplemental information of Scott and Collins (2021). Red dots show the locations of USGS stream gages where suspended sediment loads are measured (data presented in Table 3, from Anderson et al., 2019). USGS streamgages shown are: North Fork Nooksack nr Glacier, WA (12205000), Middle Fork Nooksack nr Deming, WA (12208000), South Fork Nooksack at Saxon Bridge, WA (12210000), and Nooksack River at North Cedarville, WA (12210700). Black outlines show watershed boundaries from the NHDPlus database, HU10 watersheds, and watershed names are labeled with black text. Of the basins measured in this study, only Mazama Basin feeds the stream gage in the Upper North Fork Nooksack River and only Deming and Thunder basins feed the stream gage in the Middle Fork Nooksack River.

Table S4. Reanalysis of Scott and Collins (2021) terrace erosion study. Sum of terrace erosion rates in each of the watersheds shown in Figure S6 and summed across all terrace erosion sites in the Nooksack river.

Watershed	Bluff erosion (m^3/yr)	Lower bound uncertainty	Upper bound uncertainty
Nooksack River	71084	69286	72882
Upper North Fork Nooksack River	0	0	0

Lower North Fork Nooksack River	9739	9527	9950
Middle Fork Nooksack River	0	0	0
South Fork Nooksack River	33934	32938	34931

Table S5. Descriptions of the process for reanalysis of Anderson et al. (2019), Turowski et al. (2015), Scott and Collins (2021) and data presented in this study. Results of these calculations presented in Table 3.

	Suspended Sediment Load (Anderson et al., 2019)	Inferred total load (Turowski et al., 2010)	Bluff/terrace erosion (Scott and Collins, 2021)	Proglacial total yield (This study)	Proglacial total yield (This study)
North Fork Nooksack	North Fork Nooksack nr Glacier, WA (12205000). Range presented represents two measurement periods, water years 2014-2016 and only water year 2016, both of which are presented by Anderson et al. (2019). Original measurements 220k - 260k ton/yr.	Sum of suspended sediment load (column to the left) and bedload, which is estimated based on visual interpretation of Figure 10 in Turowski et al. Gage 12205000 has drainage area of 271 km^2. Fraction suspended load ranges from 0.45 - 0.95) (bedload 0.05 - 0.55). Inferred bedload rates are calculated using the upper range of suspended sediment loads reported at left.	Originally reported in m^3/yr. Converted to tonnes using the author provided 2 tonnes/ m^3, his assumed density of measured terrace material. Reanalysis of supplemental information from Scott and Collins was performed to identify what subset of their erosion measurements fall within the North and Middle fork Nooksack river systems. Scott's and Collins' dataset is composed of measurements of individual terrace sites using georeferenced polygons and DEMs of Difference. We identified which polygons are within the the North and Middle fork river systems and summed these erosion measurements (in units of m^3).	Sediment yield of Mazama basin, 1992-2015, Table S3 (type == "all"), 789,000 m^3.	Sediment yield of Mazama basin, 1947-2015.
Middle Fork Nooksack	Middle Fork Nooksack nr Deming, WA (12208000). Range presented represents two measurement periods, water years 2014-2016 and only water year 2016?????. Original measurements 190k - 240k ton/yr.	Sum of suspended sediment load (column to the left) and bedload, which is estimated based on visual interpretation of Figure 10 in Turowski et al. Gage 12208000 has drainage area of 192 km^2. Fraction suspended load ranges from 0.4 - 0.95 (bedload 0.05 - 0.6). Inferred bedload rates are calculated using the upper range of suspended sediment loads reported at left.	Originally reported in m^3/yr. Converted to tonnes using the author provided **2 tonnes/m^3**.	Sediment yield of Deming basin, 1991-2015, Table S3 (type == "all"), 1,432,000 m^3, and Thunder basin, 1979-2015, Table S4 (named interval == 'retreat'), 3.33 kt/yr.	Sediment yield of Deming, and Thunder basins, 1947-2015.
North and Middle Forks (Main stem, less South Fork contributions)	Contributions from Nooksack River at North Cedarville, WA (12210700) minus contributions from South Fork Nooksack at Saxon Bridge, WA (12210000). Range presented represents two measurement periods, water years 2014-2016 and only water year 2016. Original measurements for the main stem are 870k - 1020k ton/yr. Original measurements for South Fork 265k - 430k ton/yr. Original measurements combining main stem less south fork are (1020k - 430k) and (870k -265k), resulting in a range 590k to 605k ton/yr	Sum of suspended sediment load (column to the left) and bedload, which is estimated based on visual interpretation of Figure 10 in Turowski et al. The main stem gage 12210700 has drainage area of 1525 km^2. The south fork gage 12210000 has drainage area 334 km^2. Subtracting the drainage area of the south fork from the main stem, drainage area is (1525 - 334) = 1191 km^2. Fraction suspended load ranges from 0.55 - 0.95 (bedload 0.95 - 0.45). Inferred bedload rates are calculated using the upper range of suspended sediment loads reported at left.	Originally reported in m^3/yr. Converted to tonnes using the author p**rovided 2 tonnes/m^3**. Original measurement from Scott and Collins for the main stem is 71,084. Reanalysis of Scott and Collins supplemental data provides calculation for South Fork of 33,934 m^3/yr. Subtracting that value from the Main Stem values result in 37,150 m^3/yr.	Sediment yield of Mazama basin, 1992-2015, 789,000 m^3; Coleman basin, 1990-2015, 320,000 m^3; Deming basin, 1991-2015, 1,432,000 m^3, all from Table S3 (type == "all"). And Thunder basin, 1979-2015, Table S4 (named interval == 'retreat'), 3,33 kt/yr.	Sediment yield of Mazama, Deming, Coleman, and Thunder basins, 1947-2015.

Figure S7. Image of the western moraine near Easton Glacier. Observations with the 1947-2015 DoD indicate that the horizontal retreat of moraines observed in Deming, Coleman, and Easton proglacial basins is due to similar processes.

Figure S8. Relationship between nonigneous fraction and other terrain characteristics for 10 basins on Mount Baker. Strong interaction is exhibited between nonigneous fraction and drainage area, hillslope domain slope, and channel slope.

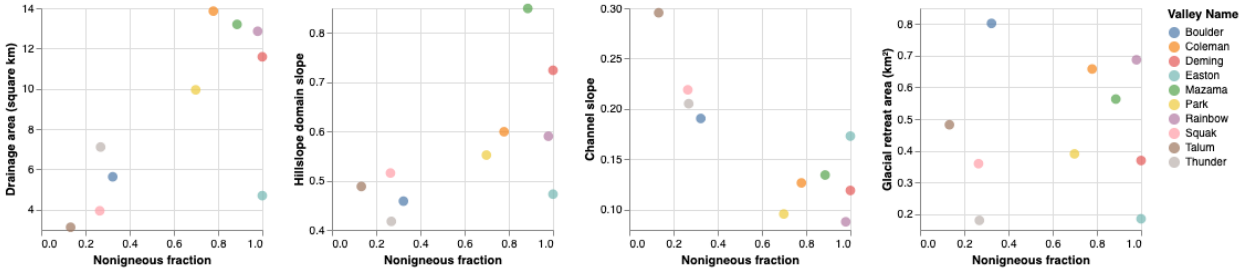

Figure S9. Showing the same data and models as in Figure 8, but with models fit only to basins with nonigneous fractions larger than 0.5 (n = 6). Relationships between terrain characteristics and mean annual sediment yields in erosional valleys of Mount Baker calculated for the 1947-2015 period (Table 2, Figure 7). Open circles represent net depositional valleys. Uncertainty for each sediment yield measurement is represented by vertical bars and values are presented in Table S4. Two gray lines are plotted, a line of best fit and a fitted geomorphic transport law (GTL). Theoretical GTL model equations and fitted GTL model equations are shown above each panel. Nash-Sutcliffe model efficiency (NSE) values are shown above each panel. For the fitted lines (linear models), NSE may be interpreted similarly to r^2.

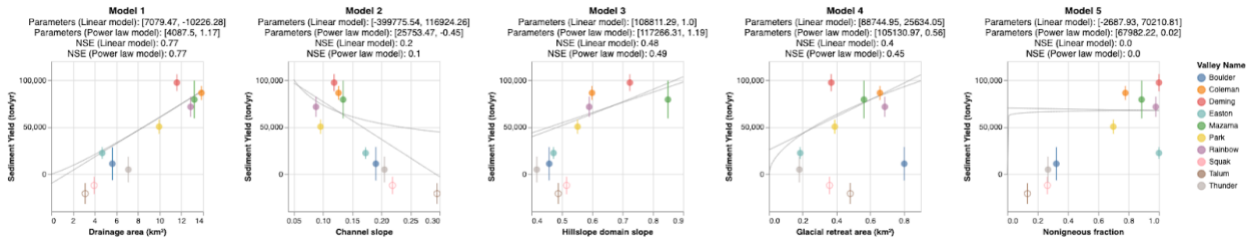

Figure S10. 1947-2015 DEM of Difference over all of Mount Baker.